Stellar-mass black holes in the Hyades star cluster?

S. Torniamenti[1,2,3]★, M. Gieles[4,5], Z. Penoyre[6,7], T. Jerabkova[8], L. Wang[9,10], F. Anders[4]
[1] Physics and Astronomy Department Galileo Galilei, University of Padova, Vicolo dell'Osservatorio 3, I–35122, Padova, Italy
[2] INFN - Padova, Via Marzolo 8, I–35131 Padova, Italy
[3] INAF - Osservatorio Astronomico di Padova, Vicolo dell'Osservatorio 5, I-35122 Padova, Italy
[4] Institut de Ciències del Cosmos (ICCUB), Universitat de Barcelona (IEEC-UB), Martí i Franquès 1, E08028 Barcelona, Spain
[5] ICREA, Pg. Lluís Companys 23, E08010 Barcelona, Spain
[6] Institute of Astronomy, University of Cambridge, Madingley Road, CB3 0HA, Cambridge, UK
[7] Leiden Observatory, Leiden University, PO Box 9513, 2300 RA, Leiden, The Netherlands
[8] European Southern Observatory, Karl-Schwarzschild-Straße 2, 85748 Garching bei München, Germany
[9] School of Physics and Astronomy, Sun Yat-sen University, Daxue Road, Zhuhai, 519082, China
[10] CSST Science Center for the Guangdong-Hong Kong-Macau Greater Bay Area, Zhuhai, 519082, China

Accepted XXX. Received YYY; in original form ZZZ

ABSTRACT

Astrophysical models of binary-black hole mergers in the Universe require a significant fraction of stellar-mass black holes (BHs) to receive negligible natal kicks to explain the gravitational wave detections. This implies that BHs should be retained even in open clusters with low escape velocities ($\lesssim 1$ km/s). We search for signatures of the presence of BHs in the nearest open cluster to the Sun – the Hyades – by comparing density profiles of direct N-body models to data from *Gaia*. The observations are best reproduced by models with 2 – 3 BHs at present. Models that never possessed BHs have an half-mass radius $\sim 30\%$ smaller than the observed value, while those where the last BHs were ejected recently ($\lesssim 150$ Myr ago) can still reproduce the density profile. In 50% of the models hosting BHs, we find BHs with stellar companion(s). Their period distribution peaks at $\sim 10^3$ yr, making them unlikely to be found through velocity variations. We look for potential BH companions through large *Gaia* astrometric and spectroscopic errors, identifying 56 binary candidates - none of which consistent with a massive compact companion. Models with 2 – 3 BHs have an elevated central velocity dispersion, but observations can not yet discriminate. We conclude that the present-day structure of the Hyades requires a significant fraction of BHs to receive natal kicks smaller than the escape velocity of $\sim 3\,\mathrm{km\,s^{-1}}$ at the time of BH formation and that the nearest BHs to the Sun are in, or near, Hyades.

Key words: black hole physics – star clusters: individual: Hyades cluster – stars: kinematics and dynamics – binaries: general – methods: numerical

1 INTRODUCTION

The discovery of binary black holes (BBH) mergers with gravitational wave (GW) detectors (The LIGO Scientific Collaboration et al. 2021) has led to an active discussion on the origin of these systems (e.g. Belczynski et al. 2016a; Mandel & de Mink 2016; Rodriguez et al. 2016; Samsing et al. 2022). A popular scenario is that BBHs form dynamically in the centres of globular clusters (GCs, e.g. Portegies Zwart & McMillan 2000; Antonini & Gieles 2020a) and open clusters (OCs, e.g. Rastello et al. 2019; Di Carlo et al. 2019; Kumamoto et al. 2020; Banerjee 2021; Torniamenti et al. 2022). This scenario has gained support from the discovery of accreting BH candidates in an extragalactic GC (Maccarone et al. 2007) and several Milky Way GCs (Strader et al. 2012; Chomiuk et al. 2013; Miller-Jones et al. 2015) as well as the discovery of three detached binaries with BH candidates in the Milky Way GC NGC 3201 (Giesers et al. 2018, 2019) and one in the 100 Myr star cluster NGC 1850 in the Large Magellanic Cloud (Saracino et al. 2022, but see El-Badry & Burdge 2022; Saracino et al. 2023).

Various studies have also pointed out that populations of stellar-mass BHs may be present in GCs, based on their large core radii (Mackey et al. 2007, 2008); the absence of mass segregation of stars in some GCs (Peuten et al. 2016; Alessandrini et al. 2016; Weatherford et al. 2020); the central mass-to-light ratio (for the cases of Omega Centauri and 47 Tucanae see Zocchi et al. 2019; Baumgardt et al. 2019; Hénault-Brunet et al. 2019); the core over half-light radius (Askar et al. 2018; Kremer et al. 2020) and the presence of tidal tails (see Gieles et al. 2021, for the case of Palomar 5).

Recently, Gieles et al. (2021) presented direct N-body models of the halo GC Palomar 5. This cluster is unusually large (~ 20 pc) and is best-known for its extended tidal tails. Both these features can be reproduced by an N-body model that has at present $\sim 20\%$ of the total mass in stellar-mass BHs. They show that the half-light radius, $R_{\rm eff}$, is a strong increasing function of the mass fraction in BHs ($f_{\rm BH}$). Because all models were evolved on the same orbit, this implies that the ratio of $R_{\rm eff}$ over the Jacobi radius is the physical parameter that is sensitive to $f_{\rm BH}$.

At the present day, all of the searches for BH populations in star clusters focused on old ($\gtrsim 10$ Gyr) and relatively massive ($\gtrsim 10^4\,\mathrm{M_\odot}$) GCs in the halo of the Milky Way and there is thus-

★ E-mail: stefano.torniamenti@unipd.it

far no work done on searches for BHs in young OCs in the disc of the Milky Way. The reason is that most methods that have been applied to GCs are challenging to apply to OCs: for mass-to-light ratio variations, precise kinematics are required, which is hampered by orbital motions of binaries (Geller et al. 2015) and potential escapers (e.g. Fukushige & Heggie 2000; Claydon et al. 2017) at the low velocity dispersions of OCs (few 100 m/s).

In the last few years, the advent of the ESA *Gaia* survey (Gaia Collaboration et al. 2016, see Gaia Collaboration et al. 2022 for the latest release) has allowed us, for the first time, to study in detail the position and velocity space of OCs (e.g., see Cantat-Gaudin 2022 for a recent review), and to identify their members with confidence. Several hundreds of new objects have been discovered (e.g. Cantat-Gaudin et al. 2018a,b; Castro-Ginard et al. 2018, 2020, 2022; Sim et al. 2019; Liu & Pang 2019; Hunt & Reffert 2021), and could be distinguished from non-physical over-densities that were erroneously listed as OCs in the previous catalogues (Cantat-Gaudin & Anders 2020).

The possibility to reveal the full spatial extension of OCs members has made it feasible to describe in detail their radial distributions, up to their outermost regions (Tarricq et al. 2022), and to study them as dynamical objects interacting with their Galactic environment. In particular, OCs display extended halos of stars, much more extended than their cores, which are likely to host a large number of cluster members (Nilakshi et al. 2002; Meingast et al. 2021). Also, evidence of structures that trace their ongoing disruption, like tidal tails, has been found for many nearby OCs, like the Hyades (Reino et al. 2018; Röser et al. 2019; Lodieu et al. 2019; Meingast & Alves 2019; Jerabkova et al. 2021), Blanco 1 (Zhang et al. 2020), Praesepe (Röser & Schilbach 2019), and even more distant ones like UBC 274 (Piatti 2020; Casamiquela et al. 2022). This wealth of data provides, for the first time, the required information to characterize the structure of OCs in detail and, possibly, to look for the imprints given by the presence of dark components, in the same way as done for GCs.

In this exploratory study, we aim to find constraints on the presence of BHs in the Hyades cluster, the nearest - and one of the most widely studied - OCs. We use the same approach as in the Pal 5 study of Gieles et al. (2021), hence a good understanding of the behaviour of $R_{\rm eff}$ at the orbit of the Hyades is required, i.e. the model clusters need to be evolved in a realistic Galactic potential. To this end, we explore the large suite of $N-$body models by Wang & Jerabkova (2021), conceived to model the impact of massive stars (i.e. the BH progenitors) on the present-day structure of Hyades-like clusters. By comparing these models to the radial profiles of Hyades members with different masses from *Gaia* (Evans & Oh 2022), we aim to constrain if a BH population is required.

The paper is organised as follows. In Section 2, we describe the details of the $N-$body models and our method to compare them to observations. In Section 3, we report the results for the presence of BHs in the Hyades. In Sect. 4 we report a discussion on BH-star candidates in the cluster. Finally, Sect. 5 summarises our conclusions.

2 METHODS

2.1 The Hyades cluster

The Hyades is the nearest OC to us, at a distance $d \approx 45$ pc (Perryman et al. 1998). By relying on 6D phase-space constraints, Röser et al. (2011) identified 724 stellar members moving with the bulk Hyades space velocity, with a total mass 435 $M_\odot$ (Röser et al. 2011). The tidal radius is estimated to be $r_{\rm t} \approx 10$ pc, and the resulting bound mass is $\approx 275\,M_\odot$ (Röser et al. 2011). Also, the cluster displays prominent tidal tails, which extend over a distance of 800 pc (Jerabkova et al. 2021).

	Plummer parameters		Stars within 10 pc	
	$M_{\rm p}$ ($M_\odot$)	$a_{\rm p}$ (pc)	M ($M_\odot$)	$r_{\rm hm}$ (pc)
Low-mass	117.3	6.21	71.9	5.67
High-mass	207.5	3.74	170.5	4.16

Table 1. Left: Total mass scale ($M_{\rm p}$) and radius scale ($a_{\rm p}$) for the two components of the best-fit Plummer model, from Evans & Oh (2022). Right: the resulting mass (M) and half-mass radius ($r_{\rm hm}$) for the stars within 10 pc, obtained by truncating the best-fit Plummer models at $r_{\rm t} = 10$ pc.

The Hyades contains stars with masses approximately between 0.1 $M_\odot$ and 2.6 $M_\odot$. Röser et al. (2011) found that average star mass of the cluster is observed to decrease from the center to the outward regions, as a consequence of mass segregation. Recently, Evans & Oh (2022) performed a detailed study of the Hyades membership and kinematics, with the aim to quantify the degree of mass segregation within the cluster. In particular, they applied a two-component mixture model to the *Gaia* DR2 data (Gaia Collaboration et al. 2018a) and identified the cluster and tail members with masses $m > 0.12\,M_\odot$ (brighter than $m_{\rm G} < 14.06$). They assigned a mass value to each observed source by means of a nearest-neighbour interpolation on the *Gaia* colour-magnitude space (BP − RP vs. $m_{\rm G}$). Finally, they defined two components, named "high-mass" and "low-mass" stars, based on a color threshold at BP − RP = 2, corresponding to 0.56 $M_\odot$. The component median masses are 0.95 $M_\odot$ and 0.32 $M_\odot$, respectively. These values were taken as nominal masses for the two components.

As a consequence of mass segregation within the cluster, Evans & Oh (2022) showed that this two-component formalism is needed to adequately describe the radial cumulative mass profiles over the entire radius range and within the tidal radius. In particular, the mass distributions of the stellar components within the tidal radius are well described by a superposition of two Plummer (1911) models. Table 1 reports the relevant parameters of the best-fit Plummer model (Evans & Oh 2022). The estimated total mass and half-mass radius of stars within 10 pc are $M_{\rm l} = 71.9\,M_\odot$ and $r_{\rm hm,l} = 5.7$ pc for the low-mass component, and $M_{\rm h} = 170.5\,M_\odot$ and $r_{\rm hm,h} = 4.16$ pc for the high-mass stars.

In this work, we will use the density profiles given by the best-fit Plummer models reported in Tab. 1 as observational points to compare to our $N-$body models. For this reason, hereafter we will refer to this best-fit profiles as to "observed profiles".

2.2 N-body models

We use the sample of $N-$body simulations introduced in Wang & Jerabkova (2021), which aim to describe the present-day state of the Hyades cluster.

The simulations are generated by using the N-body code PeTar (Wang et al. 2020a,b), which can provide accurate dynamical evolution of close encounters and binaries. The single and binary stellar evolution are included by using the population synthesis codes SSE and BSE (Hurley et al. 2000, 2002; Banerjee et al. 2020). The "rapid" supernova model for the remnant formation and material fallback from Fryer et al. (2012), along with the pulsational pair-instability supernova from Belczynski et al. (2016b), are used. In this prescription, if no material falls back onto the compact remnant after the launch of the supernova explosion, natal kicks are drawn from the distribution inferred from observed velocities of radio pulsars, that

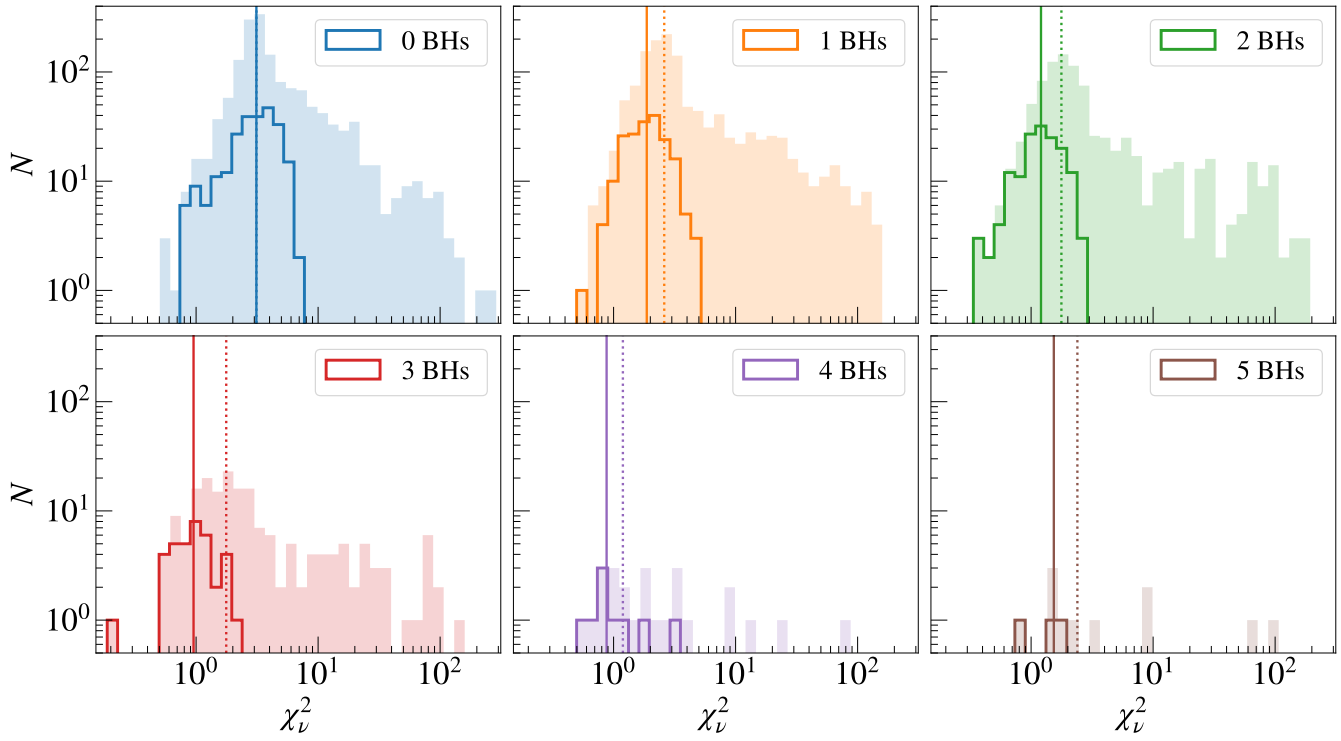

Figure 1. Distributions of χ^2_ν from the fits to the density profile for star clusters with different numbers of BHs. The filled area include the entire distributions of star clusters, while the solid line displays the star clusters with $150\,M_\odot \leq M_h \leq 190\,M_\odot$. The vertical lines show the median value of the distributions when all the clusters are considered (dotted line) and when the mass cut is applied (solid line).

is a single Maxwellian with $\sigma = 265\,\mathrm{km\,s^{-1}}$ (Hobbs et al. 2005). For compact objects formed with fallback, kicks are lowered proportionally to the amount of stellar envelope that falls back (f_b). In this case $v_{kick,fb} = (1 - f_b)v_{kick}$, where v_{kick} is the kick velocity without fallback. For the most massive BHs, which are formed via direct collapse ($f_b = 1$) of a massive star, no natal kicks are imparted. In this formalism, the kick is a function of the fallback fraction, and not of the mass of the compact remnant. In this recipe and for the adopted metallicity of $Z = 0.02$, ~ 45%(50%) of the number (mass) fraction of BHs that form has $f_b = 1$ and therefore does not receive a natal kick.

The tidal force from the Galactic potential is calculated through the GALPY code (Bovy 2015) with the MWPotential2014. This prescription includes a power-law density profile with an exponential cut-off for the bulge, a Miyamoto & Nagai (1975) disk and a NFW profile (Navarro et al. 1995) for the halo.

2.2.1 *Initial conditions*

The sample of N−body models consists of 4500 star clusters, initialized with a grid of different total masses M_0 and half-mass radii $r_{hm,0}$. The initial values for M_0 are set to 800, 1000, 1200, 1400, or 1600 $M_\odot$, while $r_{hm,0}$ takes values 0.5, 1, or 2 pc. The initial positions and velocities are sampled from a Plummer (1911) sphere.

The cluster initial mass function (IMF) is sampled from a Kroupa (2001) IMF between 0.08 − 150 $M_\odot$. For each couple $[M_0, r_{h,0}]$, Wang & Jerabkova (2021) generate 300 models by randomly sampling the stellar masses with different random seeds. On the one hand, this allows to quantify the impact of stochasticity as the result of IMF sampling, which, especially for such clusters with a limited number of particles, play a fundamental role (e.g. see Goodman et al. 1993; Boekholt & Portegies Zwart 2015; Wang & Hernandez 2021). On the other hand, different random samplings result in different fractions of O-type stars with $m > 20\,M_\odot$ (the BH progenitors), which deeply affect the cluster global evolution (see Wang & Jerabkova 2021). In the sample considered, the mass fraction of O-type stars f_O ranges from to 0 to 0.34 (the expected fraction for the chosen IMF is 0.13). The stochasticity of the mass sampling may result in clusters with $f_O = 0$, meaning that they do not contain stars massive enough to form BHs at all. The percentage of clusters with $f_O = 0$ depends on the initial cluster mass, and varies from 6% for clusters with $M_0 = 800\,M_\odot$ to 0.7% for clusters with $M_0 = 1600\,M_\odot$. Overall, 2.4% of the clusters do not host stars with $m > 20\,M_\odot$. No primordial binaries are included in the simulations (see the discussion in Section 4.1).

All the clusters are evolved for 648 Myr, the estimated age of the Hyades (Wang & Jerabkova 2021). The initial position and velocity of the cluster are set to match the present-day coordinates in the Galaxy (see Gaia Collaboration et al. 2018b; Jerabkova et al. 2021). For this purpose, the centre of the cluster is first integrated backwards for 648 Myr in the MWPotential2014 potential by means of the time-symmetric integrator in GALPY. The final coordinates are then set as initial values for the cluster position and velocity (Wang & Jerabkova 2021).

2.3 Comparing models to observations

We build the model density profiles from the final snapshots of the N−body simulations. First, we center the cluster to the density

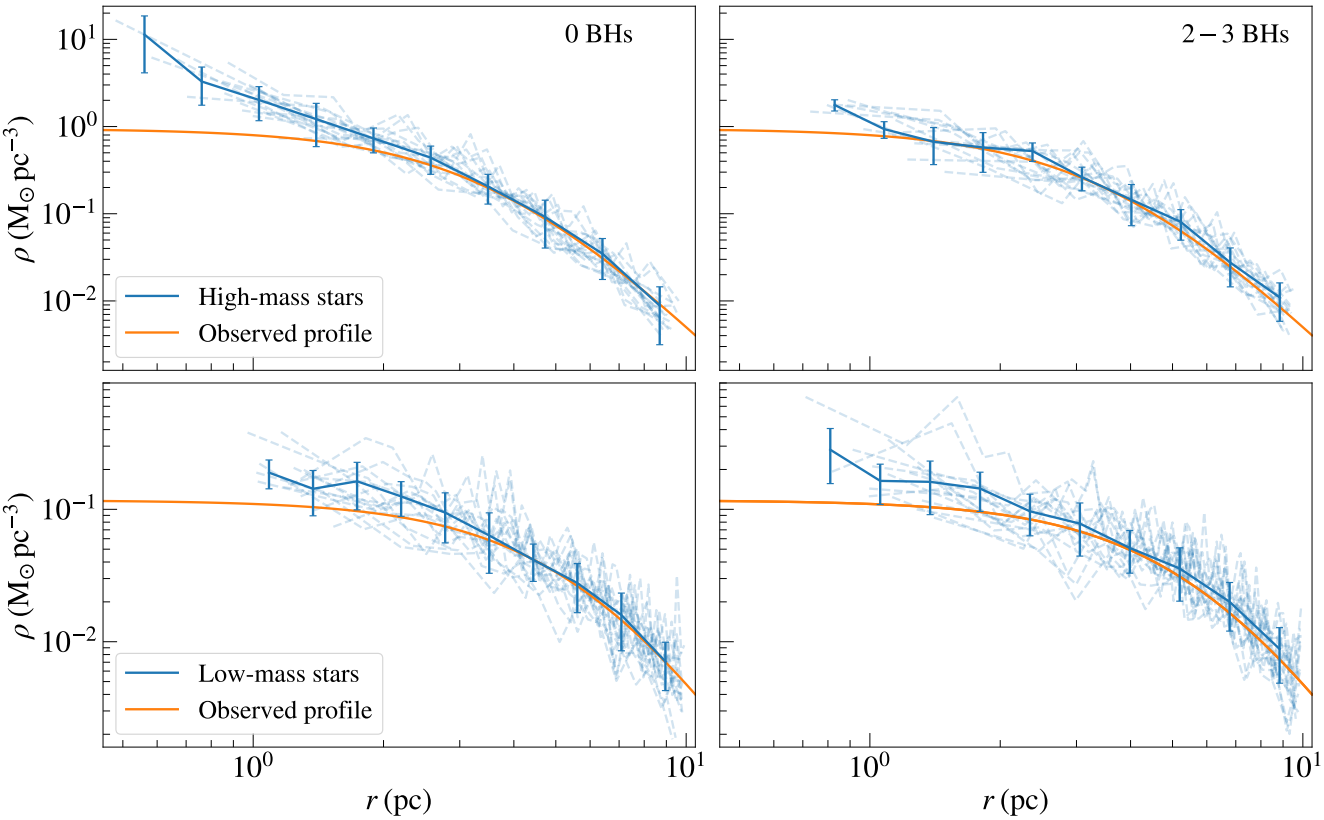

Figure 2. Density profiles for high-mass stars (upper panels) and low-mass stars (lower panels), for 16 models drawn from the cases with $N_{\rm BH} = 0$ (left) and $N_{\rm BH} = 2$ or 3 (right). The blue dashed lines are the individual models. The blue solid line is the median of the distribution at selected radial distances, with the associated errors (the Plummer uncertainties are comparable to those of the N-body models). The orange line is the observed profile (Evans & Oh 2022).

center, calculated as the square of density weighted average of the positions (Casertano & Hut 1985; Aarseth 2003). Then, we build the profiles for low-mass and high-mass stars within $r_{\rm t}$, separately. To be consistent with the observed profiles (see Sect. 2.1), we define all the stars below 0.56 $\rm M_\odot$ as low-mass stars, and all the luminous main-sequence and post-main sequence stars above this threshold as high-mass stars. Also, because we want to compare to observable radial distributions, we only include the visible components of the cluster (main sequence and giant stars), without taking into account stellar remnants, such as BHs. We divide the stellar cluster into radial shells containing the same number of stars. Due to the relatively low number of stars, we consider $N_{\rm bin} = 10$ stars per shell.

To assess how well the models reproduce the observed profiles, we refer to a chi-squared comparison, where we define the reduced chi-squared (with an expected value near 1) as:

$$\chi^2_\nu = \frac{1}{\nu}\sum_i \frac{(\rho_{{\rm obs},i} - \rho_{{\rm mod},i})^2}{\delta\rho_i^2}, \tag{1}$$

where ν is the number of degrees of freedom, which depends on the number of density points obtained with the binning procedure. The quantities $\rho_{{\rm obs},i}$ and $\rho_{{\rm mod},i}$ are the density in the $i^{\rm th}$ bin for the observed and model profile, respectively. The error $\delta\rho_i^2$ is given by the sum of the model and the observed bin uncertainties. For both observed and N−body profiles, we determine the uncertainty as the Poisson error:

$$\delta\rho = \frac{\bar{m}}{4/3\,\pi\,\left(r_f^3 - r_i^3\right)}\sqrt{N_{\rm bin}}, \tag{2}$$

where $\bar{m}$ is the mean mass of the bin stars, and r_i^3 and r_f^3 are the bin upper and lower limit. For the N−body models, the bin lower (upper) limit is set as the position of the innermost (outermost) star, and $\bar{m}$ is the mean stellar mass in each bin. For the observed profiles, we consider the same bin boundaries as the N−body models, and set $\bar{m}$ to the nominal mass of the component under consideration. Then, we estimate analytically from the Plummer (1911) distribution the number of stars between r_i and r_f.

Our comparison is performed by considering the high-mass density profile only. This choice is motivated by the fact that the observed mass function in figure 2 of Evans & Oh (2022) displays a depletion below 0.2 $\rm M_\odot$, which may hint at possible sample incompleteness. We thus focus only on the high-mass range to obtain a more reliable result. Also, high-mass stars, being more segregated, represent better tracers of the innermost regions of the cluster, where BHs are expected to reside, and thus provide more information about the possible presence of a dark component. We emphasize that this is intended as a formal analysis with the objective of determining whether a model is able to give a reasonable description of the observed cluster profile.

In order to filter out the simulations that present little agreement with the observations, we consider only the models with a final

$N_{\rm BH}$	$M_{\rm vis}$ ($M_\odot$)	$M_{\rm h}$ ($M_\odot$)	$M_{\rm tot}$ ($M_\odot$)	$f_{\rm BH}$	$f_{\rm O}$	M_0 ($M_\odot$)	$r_{h,0}$ (pc)	$P_{\rm cut}$
0 BHs	$233.9^{+21.4}_{-22.1}$	$170.5^{+12.3}_{-15.1}$	$254.0^{+24.4}_{-24.1}$	0	$0.09^{+0.06}_{-0.05}$	$1016.1^{+194.5}_{-16.1}$	$0.98^{+0.99}_{-0.48}$	13.8
1 BHs	$242.5^{+21.0}_{-21.9}$	$170.5^{+15.6}_{-10.7}$	$274.1^{+22.5}_{-25.0}$	$0.04^{+0.02}_{-0.01}$	$0.12^{+0.06}_{-0.06}$	$1201.4^{+200.3}_{-200.6}$	$0.99^{+0.99}_{-0.49}$	13.6
2 BHs	$241.2^{+21.8}_{-22.1}$	$168.1^{+14.5}_{-11.1}$	$280.2^{+22.9}_{-25.4}$	$0.07^{+0.02}_{-0.02}$	$0.15^{+0.05}_{-0.05}$	$1401.4^{+200.3}_{-200.6}$	$1.00^{+0.99}_{-0.50}$	14.2
3 BHs	$242.7^{+27.6}_{-26.2}$	$173.0^{+10.9}_{-18.0}$	$289.6^{+30.8}_{-28.4}$	$0.09^{+0.02}_{-0.01}$	$0.15^{+0.05}_{-0.04}$	$1400.5^{+195.5}_{-197.3}$	$1.96^{+0.03}_{-1.27}$	16.8
4 BHs	$249.3^{+14.2}_{-29.4}$	$167.1^{+14.1}_{-7.2}$	$294.5^{+23.7}_{-22.4}$	$0.11^{+0.02}_{-0.01}$	$0.17^{+0.03}_{-0.04}$	$1400.5^{+195.3}_{-0.2}$	$1.97^{+0.04}_{-0.71}$	27.2
5 BHs	$216.7^{+25.5}_{-8.5}$	$155.6^{+6.0}_{-3.4}$	$281.4^{+18.8}_{-14.2}$	$0.16^{+0.01}_{-0.02}$	$0.18^{+0.02}_{-0.05}$	$1598.5^{+0.3}_{-270.2}$	$1.97^{+0.00}_{-0.02}$	27.2

Table 2. Properties of the Hyades models with $150\,M_\odot \leq M_{\rm h} \leq 190\,M_\odot$, for different values of $N_{\rm BH}$ (column 1): total mass in visible stars (column 2), total mass in high-mass stars (column 3), total mass (column 4), BH mass fraction (column 5), initial mass fraction in O-type stars (column 6), initial total mass (column 7), initial half-mass radius (column 8). The last column reports the percentage of models that evolve into clusters within the mass cut, for the selected $N_{\rm BH}$. The reported values are the medians of the distributions, while the subscripts and superscripts are the difference from the 16% and 84% percentiles, respectively.

high-mass bound mass within $\pm 20\,M_\odot$ from the observed value of $M_{\rm h} = 170.5\,M_\odot$ (see Tab. 1). Among the simulated models, 636 clusters (14%) lie within this mass range.

3 RESULTS

As the cluster tends towards a state of energy equipartition, the most massive objects progressively segregate toward its innermost regions, while dynamical encounters push low-mass stars further and further away (Spitzer 1987). BHs, being more massive than most of the other stars, tend to concentrate at the cluster centre, quenching the segregation of massive stars. As a consequence, their presence in a given star cluster is expected to affect the radial mass distribution of the cluster' stellar population (Fleck et al. 2006; Hurley 2007; Peuten et al. 2016).

In the star cluster sample under consideration, the number of BHs within 10 pc, $N_{\rm BH}$, ranges from 0 to 5. Star clusters with $N_{\rm BH} = 0$ can result from the ejection of all the BHs, because of supernovae kicks (50% of the cases) and/or dynamical interactions. As for supernovae kicks, since our $N-$body models have initial escape velocities $v_{\rm esc} \lesssim 6\,{\rm km\,s^{-1}}$, which decrease to $v_{\rm esc} \lesssim 3\,{\rm km\,s^{-1}}$ at 24 Myr, only BHs formed with kicks lower than 3 km/s can be retained. Also, as mentioned earlier, the IMF may not contain massive-enough stars to form BHs (12% of the models within the mass cut that end up with 0 BHs, see Sect. 2.2).

In the following, we will assess if $N_{\rm BH} \leq 5$ BHs can produce quantifiable imprints on the radial distributions of stars.

3.1 χ^2_ν distributions

Fig. 1 shows the distributions of reduced χ^2, χ^2_ν, for different $N_{\rm BH}$. If we apply the mass cut introduced in Sect. 2.3, we can select most of the models with χ^2_ν closer to the expected value near 1, and remove those that are highly inconsistent with the observed profiles. The result of our comparison improves with increasing the number of BHs up to $N_{\rm BH} = 4$, which however exist in only 1% of the cases. If we focus on the cases with a large number of good fits ($N_{\rm BH} \leq 3$), the median value of the reduced chi-squared distributions decrease from $\chi^2_\nu \approx 3$ to $\chi^2_\nu \approx 1$ for $N_{\rm BH}$ increasing from 0 to 3.

When only models within the mass cut are considered, 98% of them have $N_{\rm BH} \leq 3$. This is mainly because star clusters that contain a high initial mass fraction in O-type stars (which evolve into BHs) are easily dissolved by the strong stellar winds (Wang & Jerabkova 2021), and result in present-day cluster masses far below the observed one. If the initial mass fraction in O-type stars is more than twice as high as that expected from a Kroupa (2001) IMF, our models cannot produce clusters in the selected mass range.

Table 2 reports the final relevant masses and mass fractions of the $N-$body models, for different values of $N_{\rm BH}$. In all the cases, the total mass in high-mass stars is $\approx 170\,M_\odot$, as a consequence of the chosen criterion for filtering out models with little agreement with the observed cluster. The total visible mass, $M_{\rm vis} \approx 240\,M_\odot$, does not show any dependence on $N_{\rm BH}$, with the only exception of the sample with 5 BHs. For the latter case, as mentioned earlier, the initial larger mass fraction of O-stars brings about a more efficient mass loss across the tidal boundary, and results in lower cluster masses. In contrast, the total mass $M_{\rm tot}$ increases with $N_{\rm BH}$: the mass in BHs spans from $\approx 10\,M_\odot$ ($f_{\rm BH} = 0.04$) when $N_{\rm BH} = 1$, to $\approx 45\,M_\odot$ for the case with 5 BHs ($f_{\rm BH} = 0.16$).

3.2 Two-component radial distributions

To highlight the difference between models with and without BHs, we randomly draw 16 models from simulations (within the mass cut) with 0 BHs and from a sample obtained by combining the sets with 2 and 3 BHs. For each distribution, we evaluated the median values for selected bins and the spread, as $1.4 \times {\rm MAD}\,\left(\sqrt{N_{\rm bin}}\right)^{-1}$, where MAD is the median absolute deviation.

Fig. 2 displays the density profiles of the high-mass (top) and low-mass (bottom) stars of these samples, compared to the observed profiles (see Sect. 2.1). The density profiles of the $N-$body models with BHs are mostly consistent with the observed distributions. High-mass stars in clusters with $N_{\rm BH} = 0$ display a more concentrated distribution reminiscent of the cusped surface brightness profiles of core collapsed GCs (Djorgovski & King 1986). The models with BHs have cored profiles, which Merritt et al. (2004) attributed to the action of a BH population. Although in our models there are only 2 or 3 BHs, it has been noticed already by Hurley (2007) that a single BBH is enough to prevent the stellar core from collapsing. It is worth noting that the Plummer models that were fit to the observations are cored and would therefore not be able to reproduce a cusp in the observed profile. But from inspecting the cumulative mass profile in

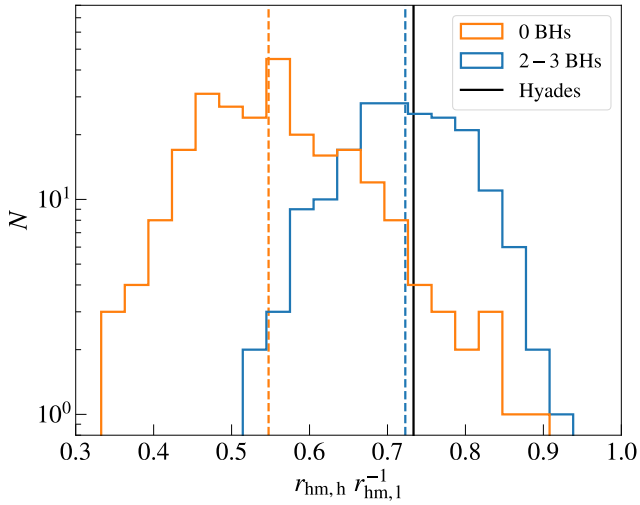

Figure 3. Ratio of the half-mass radius of the high-mass stars ($r_{\rm hm,h}$) to that of low-mass stars ($r_{\rm hm,l}$), for star clusters with $N_{\rm BH} = 0$ (orange) and $N_{\rm BH} = 2-3$ (blue). The dashed vertical lines represent the medians of the distributions, and the vertical black line displays the observed value for the Hyades (Evans & Oh 2022).

Fig. 3 of Evans & Oh (2022) we see that the observed profile follows the cored Plummer model very well, with hints of a slightly faster increase in the inner 1 pc of the high-mass components, compatible with what we see in the top-right panel of Fig. 2.

The density profile of low-mass stars is also well described by models with BHs, although they were not included in the fitting procedure. This component presents central densities lower than high-mass stars of about an order of magnitude, as a consequence of mass segregation within the cluster. A better description of the relative concentration of stars with different masses (and thus of the degree of mass segregation) is given by the ratio of their half-mass radii (e.g., see Vesperini et al. 2013, 2018; de Vita et al. 2016; Torniamenti et al. 2019). Figure 3 displays the ratio of the half-mass radius[1] of high-mass to that of low-mass stars, for all the models with 0 BHs and with 2–3 BHs. For the latter case, BHs suppress the segregation of the high-mass stars, producing less centrally concentrated distributions and increasing their half-mass radius. As a result, a lower degree of mass segregation for the visible stars is present. Also, models with BHs yield a much better agreement with the observed value.

3.3 Half-mass radii

Figure 4 shows the impact of BHs on $r_{\rm hm}$, defined as the half-mass radius of all the visible stars. The distributions shift towards higher values for increasing numbers of BHs, which is because $r_{\rm hm}$ is larger, but also because of the quenching of mass segregation of the visible components. Our models suggest that 3 BHs can produce an increase in the expected value of the half-mass radius for the visible stars of $\sim 40\%$. As a further hint on the presence of a BH component, the observed value almost coincides with the expected value for the case $N_{\rm BH} = 3$.

[1] In this study, the half-mass radii are calculated from the distributions of the stars within $r_{\rm t}$, and do not refer to the half-mass radii of the whole Plummer model.

The distribution of $r_{\rm hm}$ of the $N_{\rm BH} = 0$ sample is mostly inconsistent with the observed value of the Hyades cluster. Unlike the other cases, this distribution shows a more asymmetric shape, with a peak at $r_{\rm hm} \simeq 3$ pc, and a tail which extends towards larger values, more consistent with the models hosting BHs. We investigated if this tail may come from clusters that have recently ejected all their BHs, and have still memory of them. Figure 5 shows the the distribution of half-mass radii for the cases without BHs at the present day. We distinguished between different ranges of $t_{\rm BH}$, defined as the time at which the last BH was present within the cluster. The stellar clusters that have never hosted BHs, because they are ejected by the supernova kick or because there are not massive stars to produce them (see Sect. 3), constitute the bulk of the distribution, and are inconsistent with the observations.

The $N-$body models where all the BHs were ejected in the first 500 Myr show the same distribution as those that have never hosted BHs. For these clusters, the successive dynamical evolution has erased the previous imprints of BHs on the observable structure, because the most massive stars had enough time to segregate to the center after the ejection of the last BH. Finally, star clusters where BHs were present after 500 Myr (i.e. the last $\sim$ 150 Myr) still preserve some memory of the previous BH population, and display larger half-mass radii, in some cases consistent with the observed value. Since the present-day relaxation time (Spitzer 1987) for our $N-$body models is $t_{\rm rlx} \approx 45$ Myr, we find that the only models that have ejected their last BH less than $3\,t_{\rm rlx}$ ago have preserved some memory of their previous presence.

BHs that were ejected from the Hyades in the last 150 Myr display a median distance ~ 60 pc from the cluster (~ 80 pc from the Sun). Only in two cases, the dynamical recoil could eject the BH at a present-day distance > 1000 pc, while in all the other cases the BH is found closer than 200 pc from the cluster center.

3.4 High-mass stars parameter space

As explained in Sect. 3.3, the presence of even $2-3$ BHs has a measurable impact on the observable structure of such small-mass clusters. High-mass stars are most affected by the presence of BHs, because they are prevented from completely segregating at the cluster core. In Fig. 6 we show how the number of BHs within the cluster relates to the total mass in high-mass stars ($M_{\rm h}$) and to their half-mass radius ($r_{\rm hm,h}$). In this case, we consider all the simulated models, without any restriction on the high-mass total mass, and we show how the average number of BHs in the $N-$body models varies in the $M_{\rm h} - r_{\rm hm,h}$ space.

The total mass in high-mass stars can be as high as 400 $M_\odot$, while the half-mass radius takes values from 1 to 8 pc. The most diluted clusters feature the lowest mass, because they are closer to being disrupted by the Galactic tidal field. In contrast, models with higher $M_{\rm h}$ are characterized by the fewest BHs, because of the absence of massive progenitors, which enhance the cluster mass loss. As explained in Sect. 3.2, $r_{\rm hm,h}$ grows for increasing number of BHs at the cluster center. In the Hyades mass range, the expected value of $r_{\rm hm,h}$ when $N_{\rm BH} = 3$ is larger by almost $\sim 60\%$ with respect to the case with 0 BHs. The observed values (Evans & Oh 2022) lie in a region of the parameter space between 2–3 BHs, a further corroboration of the previous results of Sect. 3. Finally, higher numbers of BHs are disfavoured by our models, because they predict an even lower degree of mass segregation for high-mass stars.

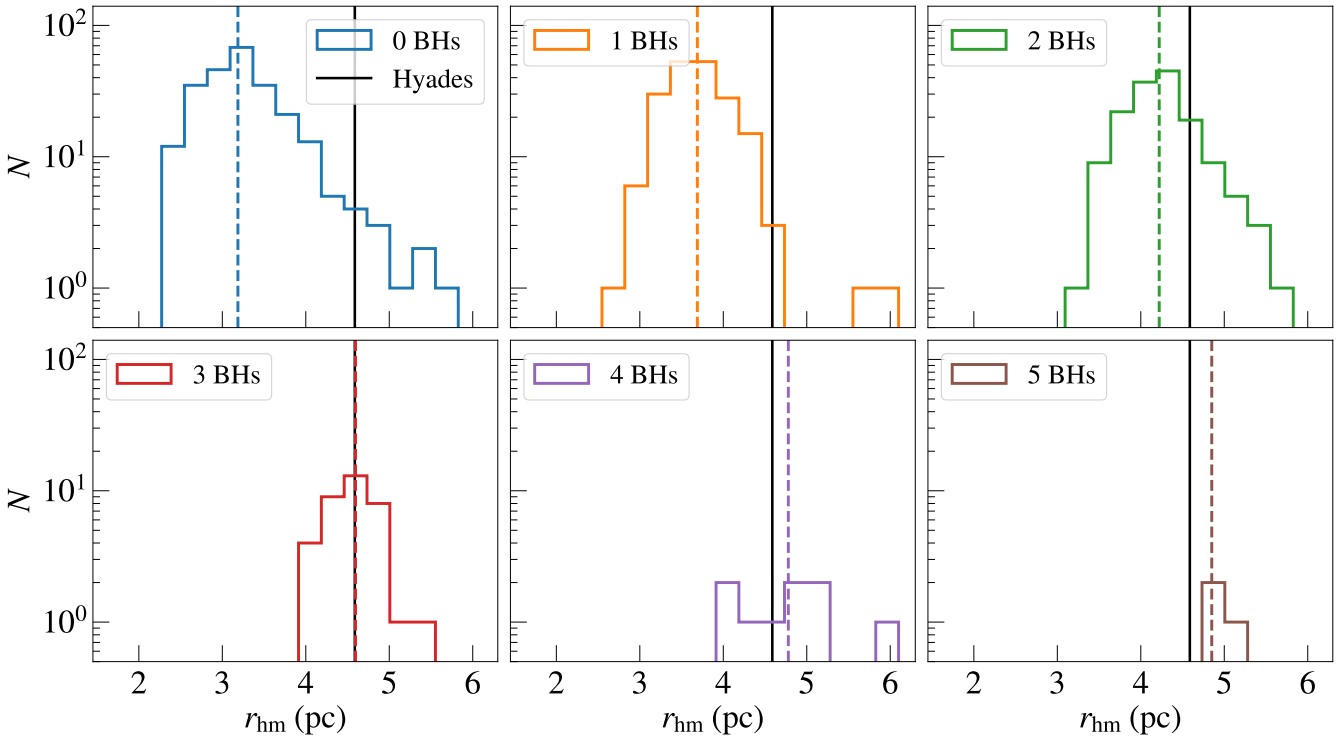

Figure 4. Distributions of half-mass radii of visible stars for N−body models with different N_{BH}. The dashed vertical lines represent the medians of the distributions, and the vertical black line displays the observed value for the Hyades (Evans & Oh 2022).

3.5 Velocity dispersion profiles

We quantified the impact of a central BH component on the velocity dispersion profile. To this purpose, we compared the same samples of 16 models with $N_{BH} = 0$ and with $N_{BH} = 2 - 3$ as done for the density profiles (see Sect. 3.2). Figure 7 displays the resulting velocity dispersion profiles, calculated as the mean of the dispersion of three velocity components. The presence of 2–3 BHs produces a non-negligible increase of 40% in the velocity dispersion in the inner 1 pc. The rise in dispersion is reminiscent of the velocity cusp that forms around a single massive object (Bahcall & Wolf 1976). Such a cusp develops within the sphere of influence of a central mass, which can be defined as $GM_\bullet/\sigma^2$, with $M_\bullet$ the mass of the central object and σ the stellar dispersion. For $M_\bullet = 20\,M_\odot$ and $\sigma = 0.3\,$km/s we find that this radius is $\sim 1\,$pc, roughly matching the radius within which the dispersion is elevated. Although a BBH of $20\,M_\odot$ constitutes $\sim$ 10% of the total cluster mass, the mass with respect to the individual stellar masses is much smaller (factor of 20) compared to the case of an intermediate-mass BH in a GC (factor of 10^4) or a super-massive BH in a nuclear cluster (factor of 10^6). As a result, a BBH in Hyades makes larger excursions from the centre due to Brownian motions. From eq. 90 in Merritt (2001) we see that the wandering radius of a BBH of $20\,M_\odot$ in Hyades is $\sim 0.15\,$pc. Although this is smaller than the sphere of influence, it is still a significant fraction of this radius. We therefore conclude that the elevated dispersion is due to the combined effect of stars bound to the BBH, stars being accelerated by interaction with the BBH (Mapelli et al. 2005) and the Brownian motion of its centre of mass.

The average increase of the velocity dispersion profile in the innermost parsec for models containing BHs indicates the potential for further validation through observations. Studies estimating the velocity dispersion of the Hyades provide central values as low as 0.3 km/s (Madsen 2003; Makarov et al. 2000), and upper limits of 0.5 km/s (Douglas et al. 2019) and 0.8 km/s (Röser et al. 2011). The Gaia data membership selection is often a trade-off between completeness and contamination and, especially for low-mass evolved star clusters, it requires a special case. For example, the data sets from Jerabkova et al. (2021) or Röser et al. (2019), who aimed to detect the extended tidal tails of the Hyades, may not be ideal for the construction of the velocity dispersion profile.

Since a detailed comparison between theoretical and observed velocity dispersion profiles requires a dedicated membership selection and a thorough understanding of the involved uncertainties, we will leave it to a follow-up focused study. Moreover, the N−body models by Wang & Jerabkova (2021) do not consider primordial binary stars (see discussion in Section 4.1), which might affect the calculated velocity dispersion.

3.6 Dynamical mass estimation

Based on the stellar mass and the velocity dispersion, Oh & Evans (2020) concluded that the Hyades is super-virial and therefore disrupting on an internal crossing timescale. The measured velocity dispersion within the cluster is commonly used to calculate the dynamical mass of the cluster, as:

$$M_{dyn} \simeq \frac{10\langle\sigma_{1D}^2\rangle R_{eff}}{G}. \quad (3)$$

We apply this our N-body model and compare it to the actual total mass. To be consistent with observations, we defined σ_{1D} as the line-of-sight velocity dispersion of high-mass stars and the effective

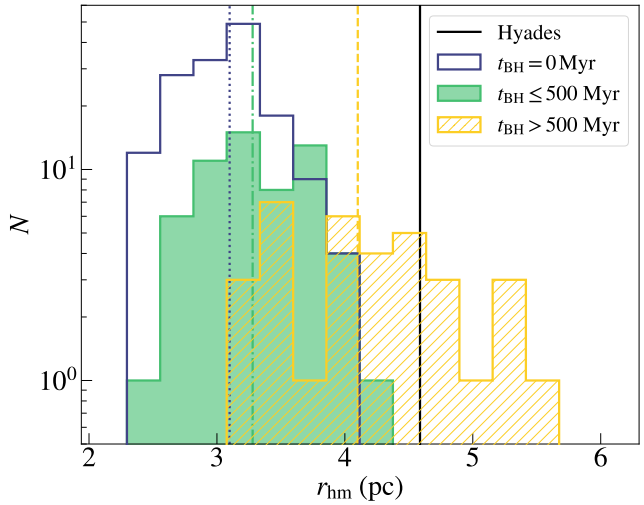

Figure 5. Distributions of r_{hm} for star clusters with no BHs. We distinguish between N−body models where BHs have never been present, because they were ejected by their natal kicks of because there were not stars massive enough in the IMF (purple, vertical dotted line), star clusters were BHs have been ejected before 500 Myr (red filled area, vertical dash-dotted line), and star clusters were BHs have been ejected after 500 Myr (yellow hatched area, vertical dashed line). The black line displays the value derived from observations (Evans & Oh 2022).

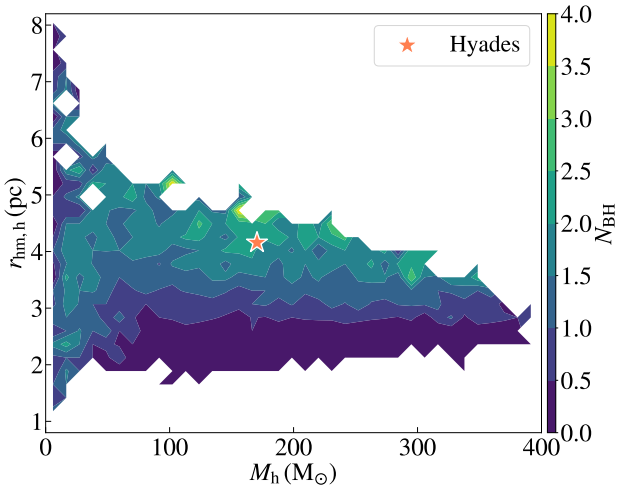

Figure 6. Contour plot of the total mass (M_h) and the half-mass radius ($r_{hm,h}$) of the high-mass stars. The colormap encodes the local mean number of BHs in that region of the parameter space. The orange star displays the values derived from observations (Evans & Oh 2022).

radius R_{eff} as the radius containing half the number of high-mass stars. We find a systematic bias of M_{dyn} overestimating the total mass of the cluster typically by a factor of $\sim$ 1.5 for $N_{BH} = 0$ and a factor of $\sim$ 2 for $N_{BH} > 0$. This is due to the presence of energetically unbound stars that are still associated with the cluster, so-called potential escapers (Fukushige & Heggie 2000), which are particularly numerous in low-mass clusters (Baumgardt 2001). N-body model of low-mass clusters with a wide mass spectrum, such a Hyades, find that the the fraction of potential escapers can be as high as 30% (Claydon et al. 2017, 2019). We therefore conclude that the high dispersion of Hyades is not because it is dissolving on a crossing time, but because it contains potential escapers and BHs.

3.7 Angular momentum alignment with BBH

The presence of a central BBH may also affect the angular momentum of surrounding stars. In particular, three-body interactions between the central BBH and the surrounding stars can lead to a direct angular momentum transfer. As a consequence, the interacting stars are dragged into corotation, and display angular momentum alignment with the central BBH (Mapelli et al. 2005). This scenario has been shown to work for BBHs with massive components ($> 50\,M_\odot$), which proved to be able to affect the angular momentum distribution for a relatively high fraction of stars. We tested this scenario for our models of the Hyades with a central BBH, where the BBH components have lower masses. In this case, stars show isotropic distribution with respect to the central BBH, independently of the distance from the cluster center. Thus, no signature of angular momentum alignment is found.

3.8 Tidal tails

The relaxation process increases the kinetic energy of stars to velocities higher than the cluster escape velocity, unbinding their orbits into the Galactic field. When this mechanism becomes effective, stellar clusters preferentially lose stars through their Lagrange points (Küpper et al. 2008), leading to the formation of two so-called tidal tails. The members of tidal tails typically exhibit a symmetrical S-shaped distribution slowly drifting away from the cluster, with over-densities corresponding to places where escaping stars slow down in their epicyclic motion (Küpper et al. 2010, 2012).

Until few years ago, tidal tails had mainly been observed in GCs (e.g., see Odenkirchen et al. 2003 for the case of Palomar 5), which are more massive, older, and often further from the Galactic plane than OCs. Thanks to the *Gaia* survey, we have now the possibility to unveil such large-scale (up to kpc) structures near OCs dissolving into the Galactic stellar field (e.g. Röser et al. 2019; Meingast & Alves 2019), thereby tracing their ongoing disruption. Identifying the tail members is critical to constrain the evolution of OCs and their interplay with the Galactic potential. Since the *Gaia* survey only provides radial velocity values for bright stars (Cropper et al. 2018), the search for tidal tail members mostly relies on projected parameters such as proper motions which have complex shapes. In this sense, mock observations from N−body models are generally adopted as a reference to recover genuine tail members, and to distinguish them from stellar contaminants (e.g., see Jerabkova et al. 2021).

Here, we focus on the impact of the present-day number of BHs on the tidal tail structure. As reported in Tab. 2, models with a larger number of BHs generally result from the evolution of more massive clusters (M_0 is $\sim$ 10% larger), as a consequence to the more efficient mass loss. This may produce a quantifiable impact on the number and density profile of the predicted tails.

Figure 8 shows the number density profiles of tidal tails from 16 models with 0 BHs and 16 models with 2−3 BHs. The median profiles and their associated uncertainties are built in the same way as for the profiles described in Sect. 3.2. To reduce the projection effects due to spatial alignment and emphasize the tail structure along the direction of the tail itself, we display the number of stars as a function of the Y

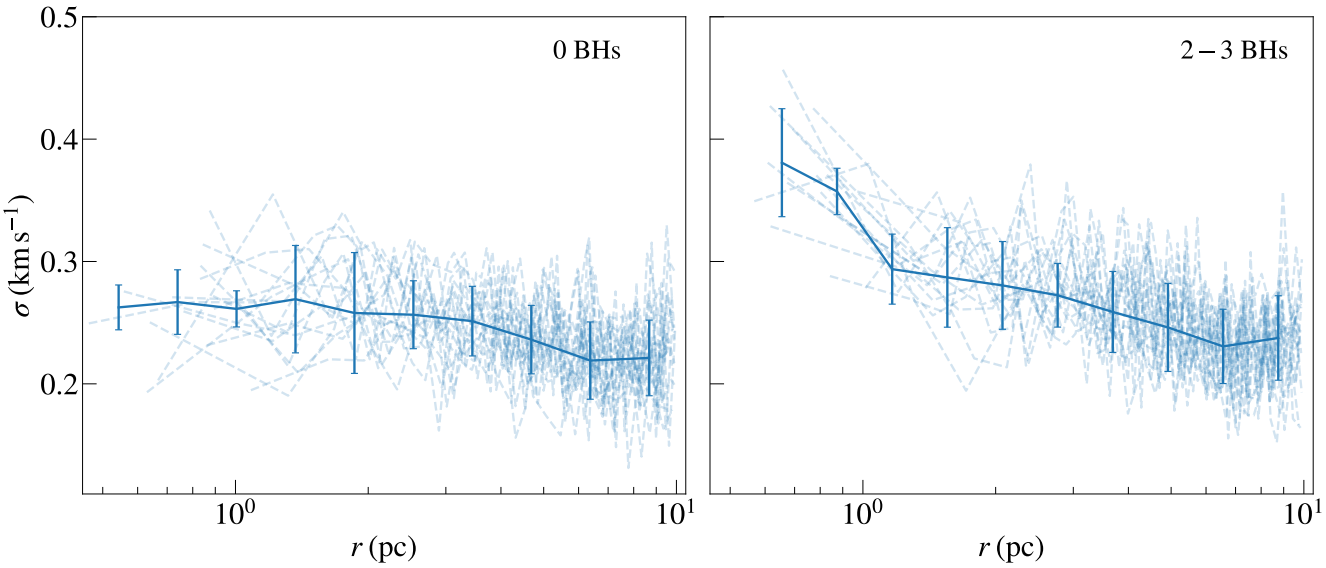

Figure 7. One-dimensional velocity dispersion profiles for 16 models drawn from the cases with $N_{\rm BH} = 0$ (left) and $N_{\rm BH} = 2-3$ (right). The blue dashed lines are the single models. The blue solid line is the median of the distribution at selected radial distances, with the associated errors.

Galactic coordinate, rotated so that the $V_{\rm Y}$ component is aligned with the tail. Also, to obtain a sample that mimics *Gaia* completeness, we consider only stars with magnitude $m_{\rm G} < 18$ mag. The profiles of models with and without BHs are almost indistinguishable, hinting at a tiny impact from the BH content. This appears in contradiction with the fact that the initial masses of the models with BHs are 50% higher than the models without BHs (see Tab. 2), while their present-day masses are similar. However, f_0 is also larger for the clusters that retain BHs, and this leads to enhanced mass-loss by winds in the first $\sim$ 50 Myr (see Fig. 5 and 7 in Wang & Jerabkova 2021). This results in models with $N_{\rm BH} = 2-3$ having a number of stars in the tails that is only $\sim$ 10% (about 200 stars) larger than those without BHs. The recent mass-loss rates of the two sets of models is comparable. The position of the epicyclic over-densities is not affected by the number of BHs (see also Fig. 8 of Wang & Jerabkova 2021).

This results means that the tidal tails of clusters as low-mass as Hyades can not be used to identify BH-rich progenitors, as was suggested from the modelling of the more massive cluster Pal 5 (Gieles et al. 2021). Future work should show whether tails of more massive OCs are sensitive to the (larger) BH content of the cluster. Also, future studies might specifically target the epicyclic over-densities in more detail and establish their phase-space properties for mode models to provide large statistical grounds. While the current observational data are not sufficient to provide such information, this will likely change with the future *Gaia* data releases and the complementary spectroscopic surveys SDSS-V (Almeida et al. 2023), 4MOST (de Jong et al. 2019) and WEAVE (Dalton et al. 2012).

4 DISCUSSION AND OBSERVATIONAL TESTS

4.1 Possible effect of primordial binaries

The $N-$body models considered for this work do not contain primordial binaries, but observations find that young star clusters have high binaries fractions, especially among massive stars (Sana et al. 2012; Moe & Di Stefano 2017). Here we discuss the possible effect of primordial binaries on the structure of clusters and, in particular, whether there may be a degeneracy with the effect of BHs.

Wang et al. (2022) investigated the impact of different mass-dependent primordial binary fractions on the dynamical evolution of star clusters with N-body simulations. Their results show that massive primordial binaries (component masses $> 5\,{\rm M}_\odot$) dominate over low-mass binaries and that the evolution of the core and half-mass radius is then insensitive to the binary fraction among low-mass stars (see Fig. 5 in Wang et al. 2022). In the absence of massive binaries, models with 100% low-mass binaries have a $\sim$ 10% larger half-mass radius than models without binaries. This difference is less than the difference we find between clusters with and without BHs.

However, the model clusters of Wang et al. (2022) are more massive ($N \sim 10^5$), so they all contain some BHs. Hurley (2007) presents N-body models of clusters without binaries and with modest binary fractions (5% and 10%). The BH natal kicks are larger in his model and BH retention is therefore rare. He finds that in models without BHs, the binary fraction does not affect the evolution of the core and half-mass radius. This was also found by Giersz & Heggie (2011) in Monte Carlo models of 47 Tucanae. Hurley (2007) showed that when two BHs are retained, the effect of the BBH that inevitably forms on the observed core and half-mass radius is far larger than the primordial binaries. In particular, his Fig. 6 shows that the model with a BBH has a central surface density that is a factor of $\sim$ 4 lower than models with binaries and without BBH. We therefore conclude that it is unlikely that a model with a modest primordial binary fraction (10%–50%) and no BHs can reproduce the Hyades profile. However, it would be interesting to verify this.

But it is equally important to consider how a high fraction of low-mass primordial would affect clusters without BHs. Figure 5 of Wang et al. (2022) shows that only clusters with a 100% binary fraction among all low-mass stars result in a similar half-mass radius as the clusters with massive binaries. Thus, we may conclude that the presence of primordial binaries does not undermine the results on BH observational signatures on this work.

In conclusion, we recognize that the presence of primordial bina-

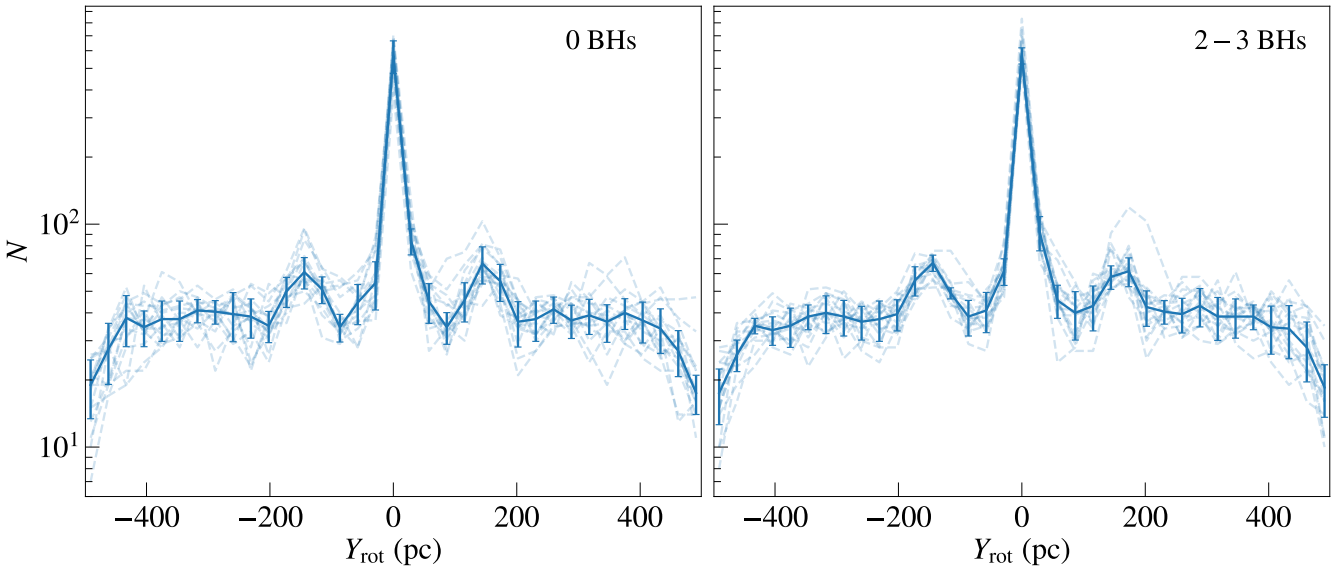

Figure 8. Tidal tail profiles for 16 models drawn from the cases with $N_{\rm BH} = 0$ (left) and $N_{\rm BH} = 2-3$ (right). The Y Galactic coordinate is rotated, so that the $V_{\rm Y}$ component is aligned with the tail. The profiles are obtained from the $N-$body models by considering all the visible stars with magnitude $m_{\rm G} < 18$.

ries play a crucial role on the long-term evolution of a cluster like the Hyades. However, a detailed characterization of the primordial binary impact on the cluster present-day structure, as well as a complete disentanglement of their observational signatures from those left by BHs, requires a more in-depth study. For this reason, we will explore it in a future work.

4.2 BH companions

Three-body interactions within a stellar cluster strongly favour the formation of binary systems, mainly composed of the most massive objects (Heggie 1975). As a consequence, BHs tend to form binaries preferentially with other BHs, and when in binaries with a lower-mass stellar companion, they rapidly exchange the companion for another BH (Hills & Fullerton 1980). In general, the result is a growing BBH population in the cluster core (Portegies Zwart & McMillan 2000). In OCs, however, given the limited number of BHs by the initial low number of massive stars, a non-negligible fraction of BH-star binary systems may form and survive.

Binary stars in dynamically-active clusters are expected to display semi-major axis distributions that depend on the cluster properties. Soft binaries (with binding energy lower than the average cluster kinetic energy) are easily disrupted by any strong encounter with another passing star or binary (Heggie 1975). The upper limit for the semi-major axis is thus given by the hard-soft boundary of the cluster:

$$a_{\rm max} = \frac{G m_1 m_2}{2\,\langle m\sigma^2\rangle}, \tag{4}$$

where $m_{1,2}$ are the masses of the binary components, and $E_{\rm b} = \langle m\sigma^2\rangle$ is the hard-soft boundary (Heggie 1975). For an OC with $\sigma \approx 0.5\,{\rm km\,s^{-1}}$, the upper limit for a binary composed of a black-hole ($m_1 = 10\,{\rm M}_\odot$) and a star ($m_2 = 1\,{\rm M}_\odot$) is of the order of $a_{\rm max} \sim 10^{-1}$ pc.

When a hard binary is formed, it becomes further tightly bound through dynamical encounters with other cluster members (Heggie 1975; Goodman 1984; Kulkarni et al. 1993; Sigurdsson & Phinney 1993). Each encounter causes the binary to recoil, until the binary becomes so tight that the recoil is energetic enough to kick it out from the cluster. For this, the lower limit $a_{\rm min}$ can be assumed to be the semi-major axis at which the binary that produces a recoil equal to the escape velocity $v_{\rm esc}$. Following Antonini & Rasio (2016):

$$a_{\rm min} = 0.2\frac{G m_1 m_2}{v_{\rm esc}^2}\frac{m_3^2}{m_{12}^2 m_{123}}, \tag{5}$$

where $m_3 = \langle m\rangle$, $m_{12} = m_1 + m_2$, and $m_{123} = m_1 + m_2 + m_3$. For an open cluster with $v_{\rm esc} \approx 0.5\,{\rm km\,s^{-1}}$, $m_1 = m_2 = 10\,{\rm M}_\odot$ and $m_3 = 0.5\,{\rm M}_\odot$, we obtain $a_{\rm min} \sim 10^{-5}$ pc (2 AU). For a BH-star binary system ($m_2 = 1\,{\rm M}_\odot$), $a_{\rm min} \sim 10^{-4}$ pc.

BHs in our $N-$body models, as expected, show a tendency to dynamically couple with other objects, and form binary and triple systems. When $N_{\rm BH} > 0$, only 6% of the BHs are not bound in a binary or multiple systems. Even in models where only 1 BH is present, the single BH tends to form binaries with (mainly) stars or other remnants (white dwarfs of neutron stars). Figure 9 shows the distribution of semi-major axes and periods for binaries and triple systems of clusters with $N_{\rm BH}$ ranging from 1 to 4. Independently of $N_{\rm BH}$, most of the binaries display semi-major axes from 10^{-5} pc to 10^{-1} pc, consistently with our approximate calculation. When more than 1 BH is present, dynamical interactions tend to favour the formation of BBHs. As reported in Tab. 3, the fraction of BBHs represents by far the largest fraction of binary systems hosting BHs if more than 1 BHs is present.

4.3 Binary candidates in the Hyades

In this section we present a search for possible massive companions to main sequence (MS) stars in the Hyades. We identify binary candidates by searching for members with enhanced *Gaia* astrometric and spectroscopic errors (following Penoyre et al. 2020; Belokurov et al. 2020, and Andrew et al. 2022).

N_{BH}	$f_{BH-Star}$	$f_{BH-Remn.}$	f_{BH-BH}
1 BHs	0.78	0.22	0.0
2 BHs	0.15	0.02	0.83
3 BHs	0.02	0.07	0.91
4 BHs	0.07	0.07	0.86
5 BHs	0.2	0.0	0.8

Table 3. Fractions of binary systems hosting BHs, for different number of BHs within 10 pc (column 1). We distinguish between different types of BH companions, specifically stars (column 2), white dwarfs or neutron stars (column 3), and BHs (column 4).

4.3.1 *Selecting cluster members*

We start with all *Gaia* DR3 sources with $\varpi > 5$ mas, RA between 62 and 72 degrees, Dec between 13 and 21 and $RUWE$, which stands for renormalized unit-weight error, greater than 0 (effectively enforcing a reasonable 5-parameter astrometric solution) - giving 5640 sources as shown in Fig. 10. We also apply an apparent G-band magnitude cut of $m_G < 15$ above which the astrometric accuracy of *Gaia* starts to degrade rapidly due to Poisson noise. Analysis beyond this magnitude is eminently possible, but for such a nearby population of stars this cut excludes a minority of the cluster (even more so the likely binary systems, as binary fraction increases with mass) and means that *Gaia* should have a near constant (~0.2 mas, Lindegren et al. 2021) precision per observation and thus allows uncomplicated comparison of sources.

To select cluster members we use the position, proper motion, and parallax to construct an (unnormalized) simple membership probability:

$$p_{\rm member} = e^{-\sum_x \left(\frac{x-x_0}{\sigma'_x}\right)^2} \tag{6}$$

where

$$\sigma'^2_x = \sigma^2_x + \sigma^2_{AEN} + \sigma^2_{x_0} \tag{7}$$

with x denoting each of the parameters of RA, Dec, $\mu_{RA^*}(=\mu_{RA}\cos(Dec))$, μ_{Dec} and ϖ. σ_x is the reported uncertainty on each parameter in the *Gaia* catalog and σ_{AEN} is the `astrometric_excess_noise` of the fit. x_0 and σ_{x_0} are the assumed values and spread of values expected for the cluster as listed in Tab. 4. The inclusion of the AEN ensures that potentially interesting binaries, which may have a significantly larger spread in their observed values and thus fall outside of the expected variance of the cluster, are not selected against.

The value of $p_{\rm member}$ for stars in the field is shown in Fig. 11 from which we choose a critical value of $\log_{10}(p_{\rm member}) = -1.75$ giving 229 members which can be seen and identified on the Hertzsprung-Russell diagram shown in Fig. 12.

4.3.2 *Astrometric and spectroscopic noise*

Following the method introduced in Andrew et al. (2022), we can use the astrometric and spectroscopic noise associated with the measurements in the *Gaia* source catalog (which assumes every star is single) to identify and characterize binary systems. This is possible for binaries with periods from days to years, as these can show significant deviations from expected single-body motion. As *Gaia* takes many high-precision measurements, the discrepancy between the expected and observed error behavior is predictable and, as we will do here, can be used to estimate periods, mass ratios and companion masses.

The first step is to select systems with significant excess noise. For astrometry, we can use a property directly recorded in the catalog $RUWE$. This is equal to the square root of the reduced chi-squared of the astrometric fit and should, for well-behaved observations, give values clustered around 1. Values significantly above 1 suggest that either the model is insufficient, the error is underestimated, or there are one or more significant outlying data points. Given that binary systems are ubiquitous (a simple rule-of-thumb is that around half of most samples of sources host more than one star, see e.g. Offner et al. 2022), these will be the most common cause of excess error, especially in nearby well-characterized systems outside of very dense fields.

It is possible to compute a reduced-chi-squared for any quantity where we know the observed variance, expected precision, and the degrees of freedom - and thus we can find the $RUWE$ associated with spectroscopic measurements as well. To do this we need to estimate the observational measurement error, which we do as a function of the stars' magnitude and color (as detailed in Andrew et al. 2022) giving $\sigma_{spec}(m_G, m_{BP} - m_{RP})$, the uncertainty expected for a single measurement for each source. Thus we can construct a spectroscopic renormalized unit-weight error, which we'll call $RUWE_{spec}$ to use alongside the astrometric which we'll denote as $RUWE_{ast}$. These values are shown for Hyades candidate members in Fig. 13.

Only a minority of *Gaia* sources have radial-velocity observations, which can be missing because sources are too bright ($m_G \lesssim 4$, as seen at the top of the HR diagram), too dim ($m_G \gtrsim 14$, as seen at the bottom), in too dense neighborhoods, or if they are double-lined (with visible absorption lines in more than one of a multiple system, as may be the case with some likely multiple stars above the main-sequence). We use only systems with `rv_method_used = 1` as only these are easily invertible to give binary properties (Andrew et al. 2022 for more details).

The particular value at which $RUWE$ is deemed significant must be decided pragmatically, and we adopt the values from Andrew et al. (2022) of $RUWE_{ast} > 1.25$ and $RUWE_{spec} > 2$, where the higher criteria for spectroscopic measurements stems from the smaller number of measurements per star and thus the wider spread in $RUWE$. We select sources satisfying both of these criteria as candidate Hyades binaries, giving 56 systems.

There are some sources that exceed one of these criteria and not the other, and these are interesting potential candidates, but they cannot be used for the next step in the analysis. Using both (generally independent) checks should significantly reduce our number of false positives. It is worth noting that radial-velocity signals are largest for short-period orbits, whereas astrometric signals are largest for systems whose periods match the time baseline of the survey (34 months for *Gaia* DR3). This both tells us about which systems we might miss or might meet one criterion and not the other. It also gives the explanation for one of the largest sources of contaminants in this process: triples (or higher multiples) where each significant excess noise comes from a different orbit and thus the two cannot be easily combined or compared.

If we know the $RUWE$ and the measurement error, and assume that all excess noise comes from the contribution of the binary we can invert to find specifically the contribution of the binary:

$$\sigma_{b,spec} = \sqrt{RUWE^2_{spec} - 1} \cdot \sigma_{spec}(m_G, m_{BP} - m_{RP}). \tag{8}$$

and

$$\sigma_{b,ast} = 2\sqrt{RUWE^2_{ast} - 1} \cdot \sigma_{ast}(m_G) \tag{9}$$

where the factor of 2 comes from the fact that *Gaia* takes one-dimensional measurements of the stars 2D position.

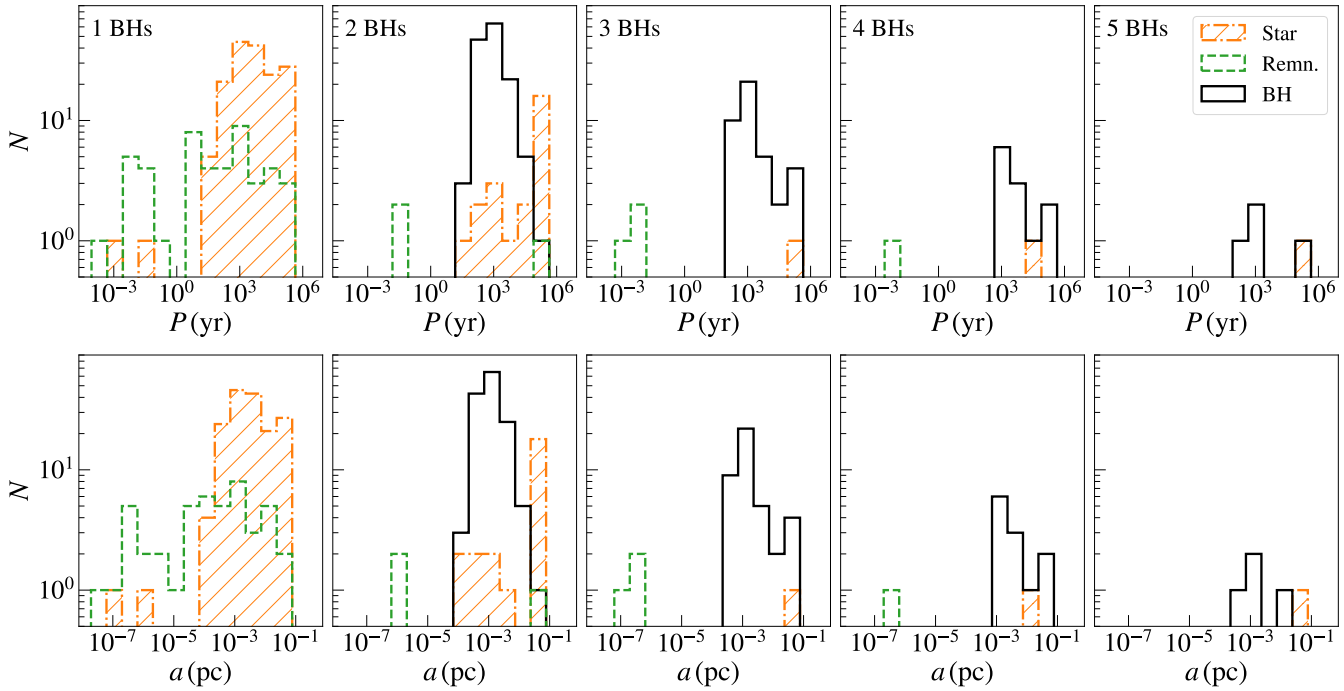

Figure 9. Distributions of periods (upper panels) and semi-major axes (lower panels) of the binary and triple systems hosting BHs, for N−body models with different numbers of BHs. We distinguish between different types of BH companions, specifically stars (orange dash-dot line, hatched area), white dwarfs or neutron stars (green dashed line), and BHs (black).

	ϖ	RA	Dec	μ_{RA^*}	μ_{Dec}
x_0	22	66.9	16.4	105	-25
σ_{x_0}	7	3.2	3.2	35	30

Table 4. Values for ϖ, RA, Dec, μ_{RA^*}, μ_{Dec}, and their reported uncertainty in the *Gaia* catalog.

4.3.3 *Binary properties from excess error*

The contributions in equations (8) and (9) can be mapped back to the properties of the binary and inverted to give the period and (after estimating the mass of the primary) the mass of the companion, as detailed in Andrew et al. (2022). For binary periods less than or equal to the time baseline of the survey the period is approximately:

$$P = \frac{2\pi A}{\varpi}\frac{\sigma_{b,ast}}{\sigma_{b,spec}}, \tag{10}$$

and the mass ratio follows:

$$q^3 - \alpha q^2 - 2\alpha q - \alpha = 0, \tag{11}$$

where

$$\alpha = \frac{A}{GM\varpi}\sigma^2_{b,spec}\sigma_{b,ast} \tag{12}$$

and $A = 1$ AU. M is the mass of the primary star which can be estimated via:

$$M = 10^{0.0725(4.76-m_G)}, \tag{13}$$

where m_G is the absolute magnitude of the star (Pittordis & Sutherland 2019). This is only strictly relevant for MS stars - but all evolved systems in the Hyades are too bright for *Gaia* spectroscopic measurements and thus will not be included in later analysis (with the exception of white dwarfs, which are too dim).

These equations assume the companion has negligible luminosity of its own. If this assumption doesn't hold then the period is slightly overestimated and the mass ratio (and companion mass) are slightly underestimated (see Fig. 3 of Andrew et al. 2022 for more detailed behaviour). The inferred properties of all 56 systems are shown in Fig. 14 and recorded in Tab. 5.

There are some simple consistency checks we can apply to these results. Primarily we know that astrometric measurements should only be discerning for binaries with periods from months to decades (Penoyre et al. 2022) - thus any deep blue or deep red points are likely spurious solutions - though there are only a handful that have erroneous seeming periods.

As we are searching for significant-mass BHs it is interesting to interrogate the sources with the highest values of q and M_c, but we should be careful as this is equivalent to selecting those with the largest errors and thus possibly those most likely to truly be erroneous (rather than caused by a binary). For example, the highest mass ratio ($q > 1$) sources are amongst the dimmest (and thus least reliably measured) in the sample - these could be physical, most likely white dwarf companions - but could also be random error.

The brighter stars that show evidence of companions have relatively modest properties - mass ratios below 1 and companion masses significantly below those of a clear BH companion.

Given the period constraints on binaries including BHs present in the simulations, as presented in Fig. 9, it is not shocking that we do not find any likely companions. We certainly cannot rule out that these or other stars in the Hyades might have massive compact companions on smaller or wider orbits that *Gaia* would be insensitive to. Instead, we are pleased to be able to present a list of candidate binaries whose companions are most likely similar main-sequence stars or white dwarfs.

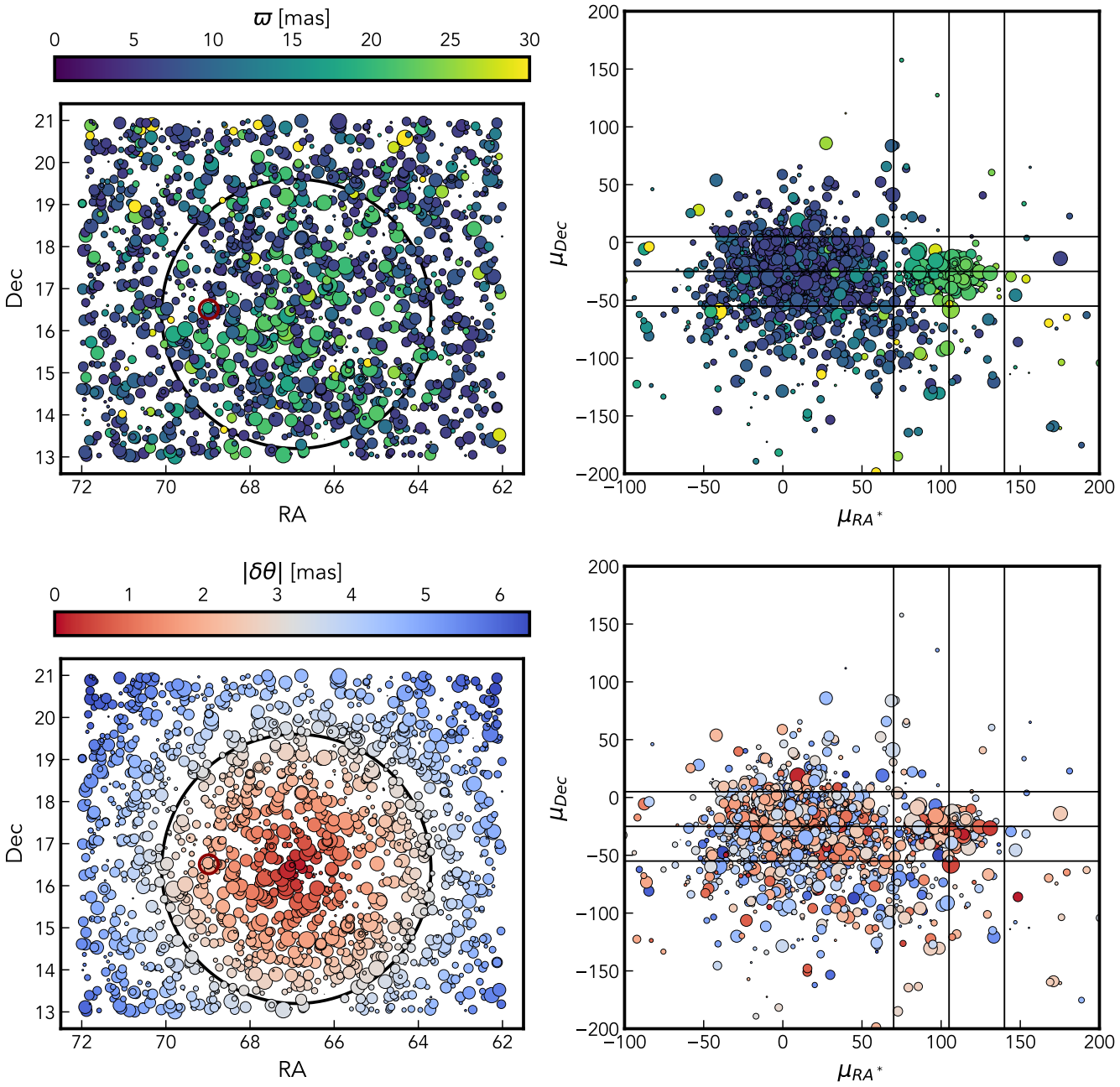

Figure 10. Position on sky (left) and proper motion (right) of sources in the field of the Hyades (with $\varpi > 5$ mas). We show the parallax (top row) and angular offset from the center of the cluster (bottom row). Aldebaran, a foreground star too bright for *Gaia*, is shown as a red open circle. The size of each point is set by their apparent magnitude and only sources with $m_G < 15$ are shown (see Fig. 12 for reference). We also show an angular offset of 3.2 mas (black circle, left) and lines denoting $\mu_{RA^*} = 105$ mas yr^{-1} and ± 35 mas yr^{-1} from this (black vertical lines, right) and $\mu_{Dec} = -25$ mas yr^{-1} and ± 30 mas yr^{-1} (black horizontal lines, right).

Stars with massive companions may still be identifiable via their velocity offset. The orbital velocity of a $1.5\,M_\odot$ star in a binary with a companion of $15\,M_\odot$ and a period of $10^3(10^4)$ yr has an orbital velocity of $\sim 7(3)$ km/s. Searching for these systems from velocity offsets is beyond the scope of this work but is an interesting avenue for future exploration.

4.4 Implications for gravitational waves

Given the vicinity of the Hyades, it is interesting to ask the question whether a BBH in the Hyades would be observable as a continuous gravitational wave source with ongoing or future experiments. Let us therefore adopt a BBH with component masses of $m_1 = m_2 = 10\,M_\odot$, an average stellar mass of $\langle m \rangle = 0.5\,M_\odot$ and an escape velocity from the centre of the cluster of $v_{\rm esc} = 0.5$ km/s. Then we assume that the semi-major axis is $a = a_{\rm min} = 2$ AU, i.e. the minimum before it is

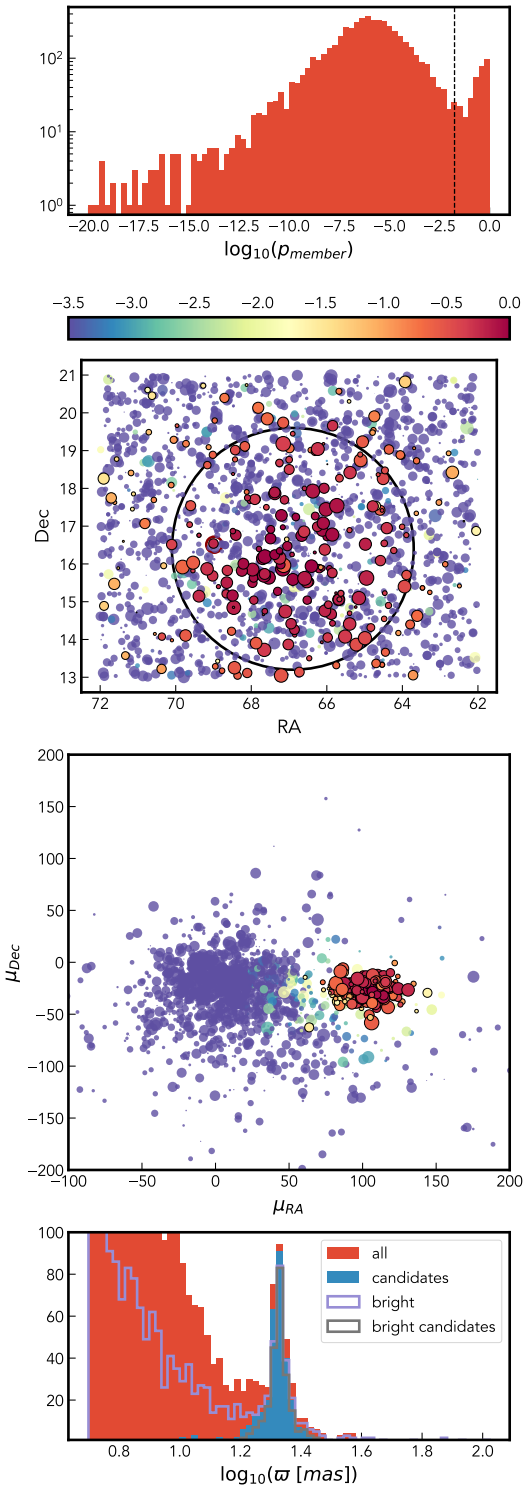

Figure 11. The cluster membership probability for stars in the Hyades field based on equation 6. We show the distribution of probabilities for all stars (top) and based on this make a cut at $\log_{10}(p_{\rm member}) = -1.75$ (vertical dashed line), We then show the position and proper motion distribution (middle two panels, similar to Fig. 10) colored by $\log_{10}(p_{\rm member})$. Stars with values greater than -1.75 are shown with black outlines. Finally, we show the parallax distribution of all stars in our field and our candidates (bottom).

ejected in an interaction with a star (equation 4.2). This is the most optimistic scenario, because it results in the smallest a, but since the interaction time between stars and the BBH goes as $1/a$, a BBH spends a relatively long time at this final, high binding energy. An estimate of the absolute duration can be obtained from the required energy generation rate (Antonini & Gieles 2020b), from which we find ~ 5 Gyr. Because this is much longer than the Hyades' age, it is a reasonable assumption that a putative BBH is near this highest energy state. For the adopted parameters, $a_{\rm min} \simeq 2$ AU. For a typical eccentricity of ~ 0.7, the peak frequency ($\sim 5 \times 10^{-4}$ mHz, equation 37 in Wen 2003), i.e. below the lower frequency cut-off of LISA (~ 0.1mHz) and the orbital period of ~ 0.7 yr is comparable to the maximum period that can be found by LISA (~ 0.7 yr, Chen & Amaro-Seoane 2017). Only for eccentricities $\gtrsim 0.99$ (2% probability for a thermal distribution) the peak frequency is $\gtrsim 0.1$ mHz. BH masses ($\gtrsim 30\,{\rm M}_\odot$) result in orbital periods comfortably in the regime that LISA could detect ($\lesssim 0.08$ yr), but such high masses are extremely unlikely given the high metallicity of the Hyades.

Because of the low frequency, we consider now whether a BBH in Hyades is observable with the Pulsar Timing Array (PTA). Jenet et al. (2005) show that a BBH at a minimum distance to the sight line to a millisecond pulsar (MSP) of 0.03 pc (~ 3 arcmin for the Hyades' distance) causes a time-of-arrival fluctuation of 0.2-20 ns, potentially observable (van Straten et al. 2001). Unfortunately, the nearest MSP in projection is PSR J0407+1607 at 5.5 deg[2]. If the BBH was recently ejected, it may be close to a MSP in projection, but the maximum distance a BBH could have travelled is ~ 1 deg (Section 3.2) and there are only 4 pulsars within a distance of 10 deg, so this is unlikely as well. In conclusion, it is unlikely that (continuous) gravitational waves from a BBH in or near the Hyades will be found.

4.5 Gravitational microlensing

Because of the vicinity of the Hyades, BHs have relatively large Einstein angles and we may detect a BH or a BBH through microlensing. For a BH mass of $10\,{\rm M}_\odot$ at a distance of 45 pc and a source at 5 kpc, the Einstein angle is $\theta_{\rm E} \simeq 40$ mas. Assuming that background stars in the galaxy are distant enough to act as a source, we find from the *Gaia* catalogue that the on-sky density of background sources is $\Sigma_{\rm S} \simeq 10^{-9}\,{\rm mas}^{-2}$. The Hyades moves with an on-sky velocity of $v_{\rm H} \simeq 100\,{\rm mas\,yr}^{-1}$ relative to the field stars. This gives us a rough estimate of the microlensing rate of $R \simeq 2\theta_{\rm E} N_{\rm BH} \Sigma_{\rm S} v_{\rm H} \simeq 2 \times 10^{-5}\,{\rm yr}^{-1}$, where we used $N_{\rm BH} = 2$. Even if we consider astrometric lensing, for which the cross section for a measureable effect is larger (e.g. Paczynski 1996; Miralda-Escude 1996), the expected rate is too low. This is mainly because of the low number of background sources because of Hyades' location in the direction of the Galactic anticentre. Perhaps the orders of magnitude higher number of stars that will be found by LSST can improve this. More promising in the short term is to search for BHs in other OCs which are projected towards the Galactic centre.

5 CONCLUSIONS

In this study, we present a first attempt to find dynamical imprints of stellar-mass black holes (BHs) in Milky Way open clusters. In particular, we focused on the closest open cluster to the Sun, the

[2] ATNF Pulsar Catalog by R.N. Manchester et al., at http://www.atnf.csiro.au/research/pulsar/psrcat

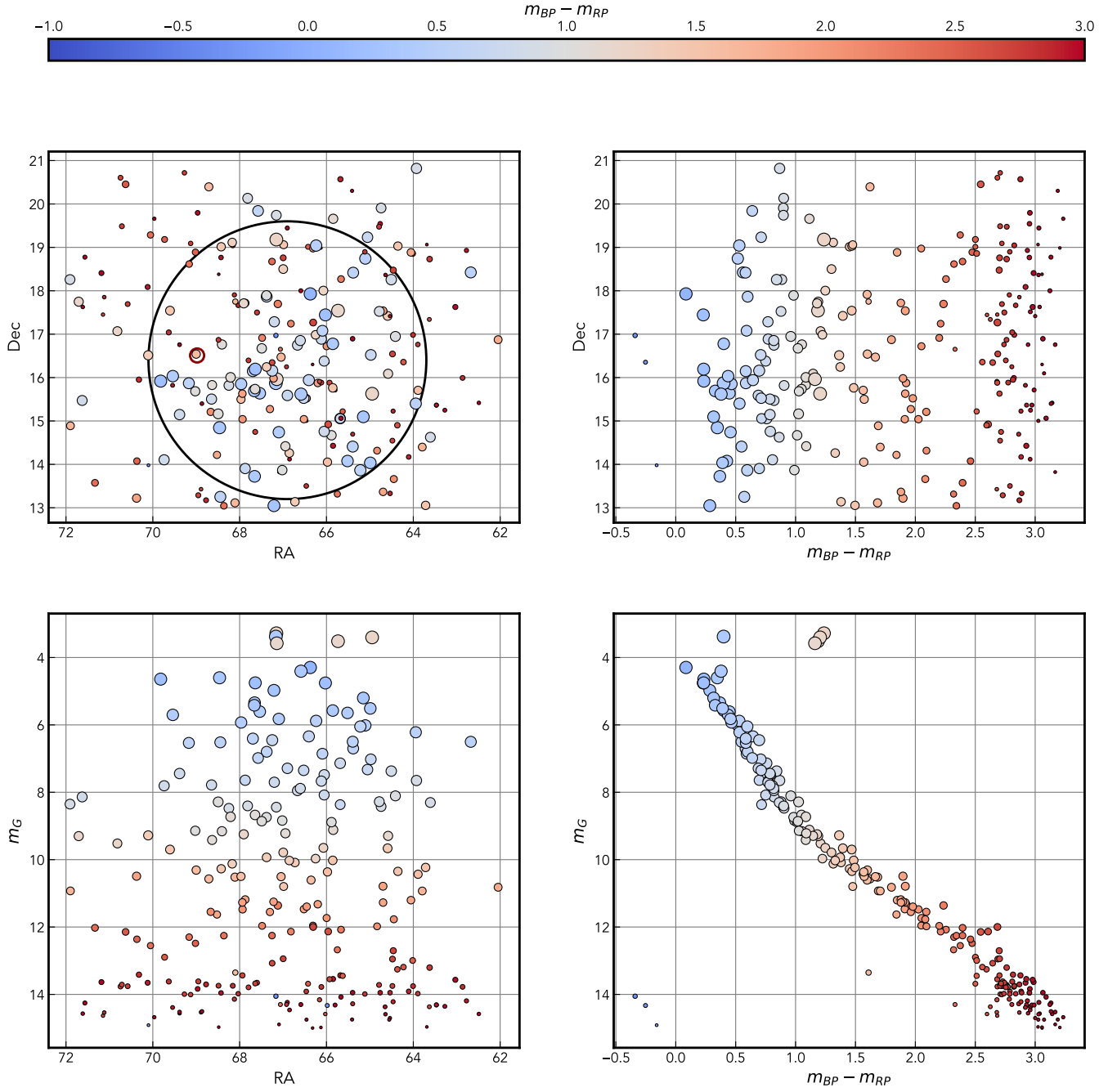

Figure 12. Sky maps and color-magnitude diagrams for the Hyades candidates, colored by *Gaia* color. Axes are shared moving horizontally and vertically between panels such that any individual star can be traced between plots.

Hyades cluster. We compared the mass density profiles from a suite of direct $N-$body models, conceived with the precise intent to model the present-day state of Hyades-like clusters (Wang & Jerabkova 2021), to radial mass distributions of stars with different masses, derived from *Gaia* data (Evans & Oh 2022).

Our comparison favors $N-$body models with $2-3$ BHs at present. In these models, the presence of a central BH component quenches the segregation of visible stars, and leads to less concentrated distributions. Star clusters with $2-3$ BHs (and a BH mass fraction $f_{\rm BH} \simeq 0.1$) best reproduce the observed half-mass radius, while those that never possessed BHs display a value that is $\sim 30\%$ smaller. This result is further confirmed by the radial distribution of high-mass stars ($m \geq 0.56\,{\rm M}_\odot$), which, being more segregated, are more affected by the presence of central BHs. Models in which the last BH was ejected recently (≤ 150 Myr ago) can still reproduce the density profile. For these model, we estimate that the ejected (binary) BHs are at a typical distance of ~ 60 pc from the Hyades.

Models with $2-3$ BHs have a one-dimensional dispersion in the innermost parsec of ~ 350 m/s compared to ~ 250 m/s for the no BH

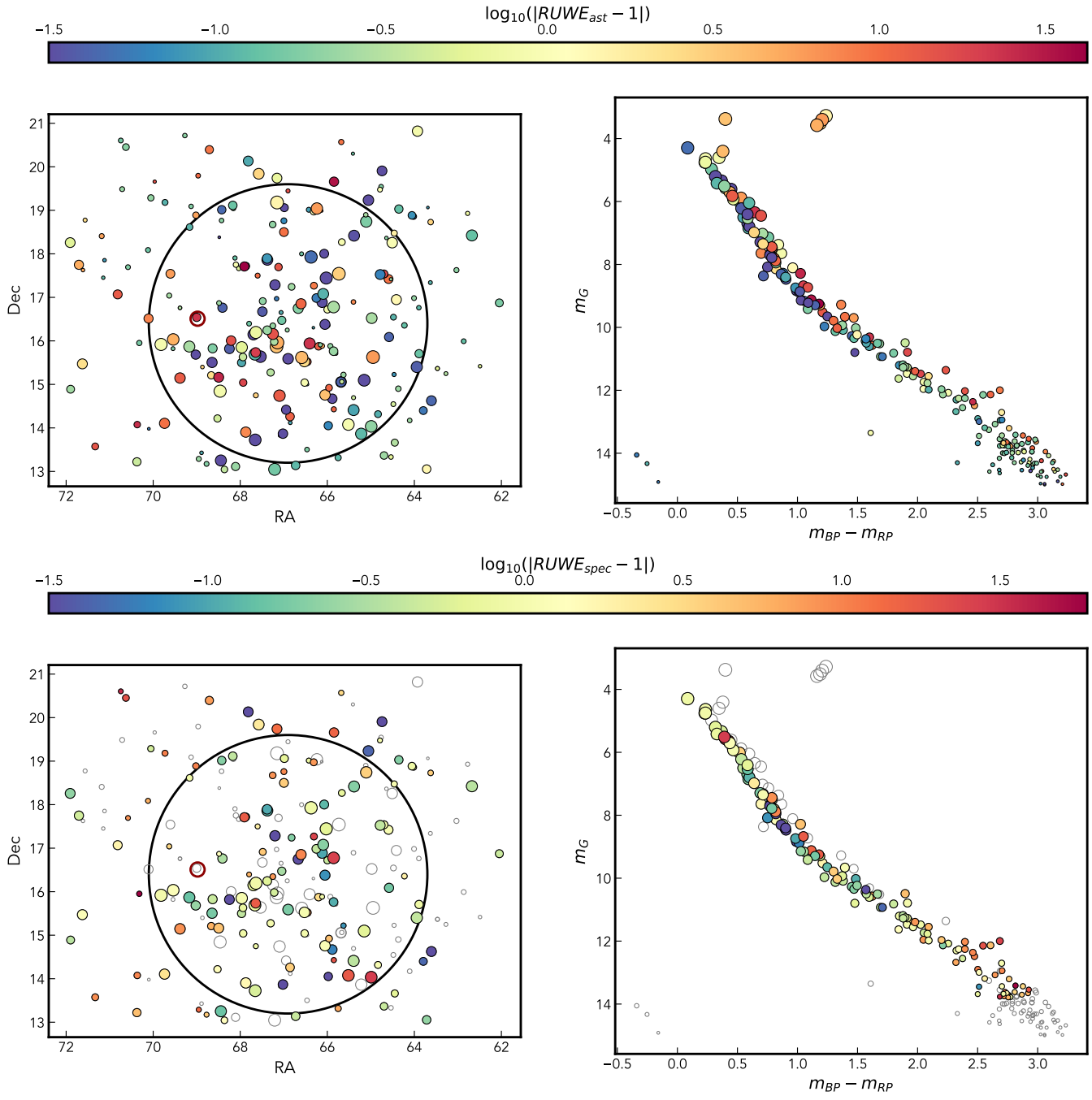

Figure 13. Hyades candidates colored by astrometric (top) and spectroscopic (bottom) renormalized-unit-weight-error ($RUWE$). Values significantly above 1 suggest that the system has an extra source of noise, most ubiquitously a binary companion. Many sources don't have radial velocity measurements in the *Gaia* source catalog, and these are denoted with empty grey circles in the bottom plot.

case and both are consistent with the available data. The tidal tails of models with and without BHs are almost indistinguishable.

In absence of primordial binaries, about 94% of the BHs in the present-day state of our $N-$body models dynamically couple with other objects and form binary and triple systems. Among them, 50% of the clusters with BHs host BH-star binary systems. Their period distribution peaks at $\sim 10^3$ yr making it unlikely to find BHs through velocity variations. We explored the possible candidate stars with a BH companion, based on their excess error in the *Gaia* singe-source catalog but otherwise high membership probability. We found 56 possible binaries candidates, but none which show strong evidence of sufficient companion mass to be a likely BH. Also, we explored the possibility to detect binary BHs through gravitational waves with Pulsar Timing Array. We found that (continuous) gravitational waves from a BBH in or near the Hyades is unlikely to be found. Finally, we estimated that detecting dormant BHs with gravitational microlensing is unlikely too.

Our study suggests that, at the present day, the radial mass dis-

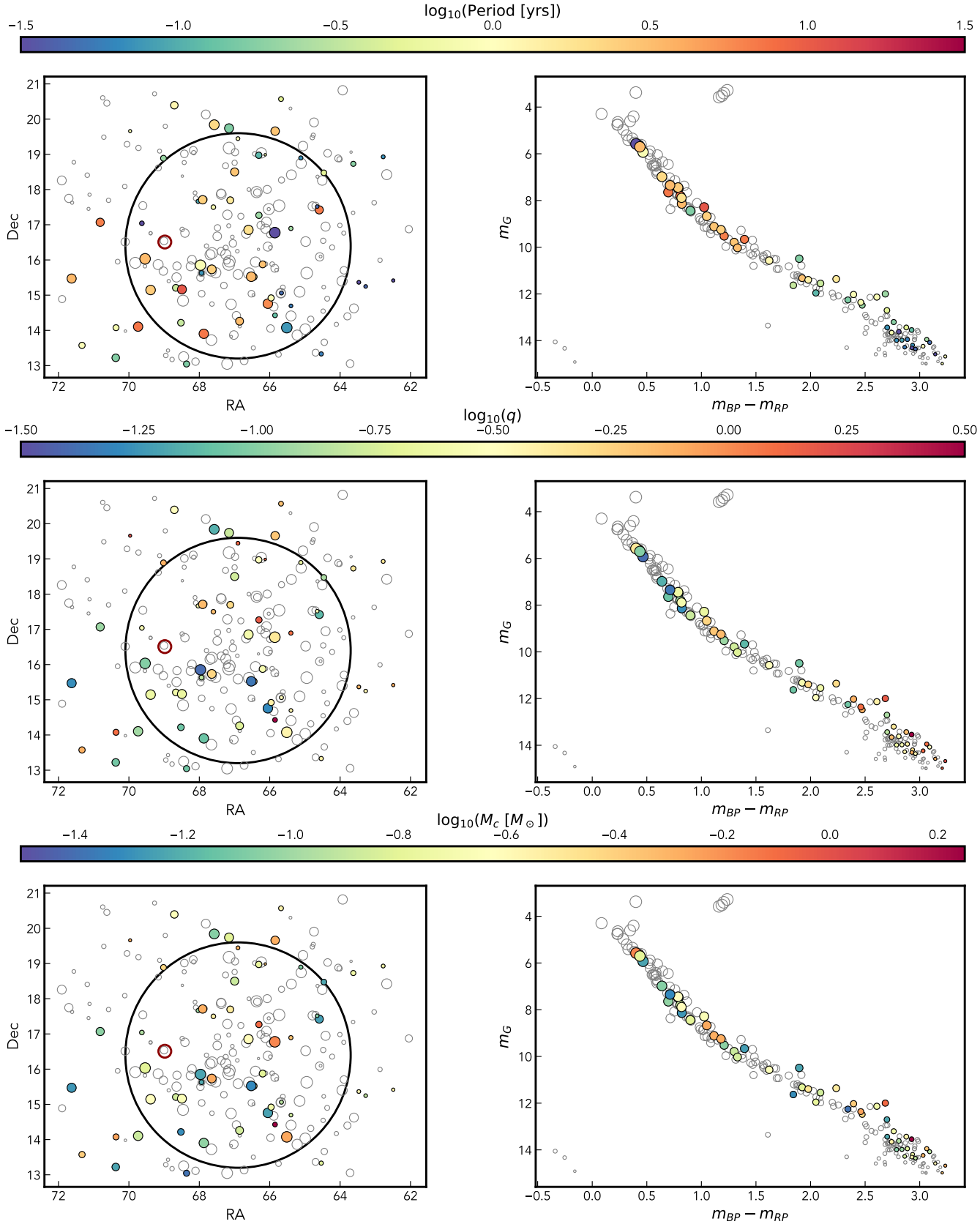

Figure 14. Periods, mass ratios (q) and companion masses (M_c) of Hyades candidates inferred from astrometric and spectroscopic $RUWE$. Only sources with significantly high $RUWE$ in both measurements are included here, and all others are shown with empty grey circles.

tribution of stars provides the most promising discriminator to find signatures of BHs in open clusters. In particular, the most massive stars within the cluster, and their degree of mass segregation, represent the best tracers for the presence of central BHs. For the case of the Hyades, its present-day structure requires a significant fraction of BHs to form with kicks that are low enough to be retained by the host cluster.

Our approach of detailed modelling of individual OCs can be applied to other OCs to see whether Hyades is an unique cluster, or that BHs in OCs are common. Charting the demographics in OCs in future studies will be a powerful way to put stringent constraints on BH kicks and the contribution of OCs to gravitational wave detections.

ACKNOWLEDGEMENTS

ST acknowledges financial support from the European Research Council for the ERC Consolidator grant DEMOBLACK, under contract no. 770017. MG acknowledges support from the Ministry of Science and Innovation (EUR2020-112157, PID2021-125485NB-C22) and from Grant CEX2019-000918-M funded by MCIN/AEI/10.13039/501100011033 and from AGAUR (SGR-2021-01069). ZP acknowledges that this project has received funding from the European Research Council (ERC) under the European Union's Horizon 2020 research and innovation programme (Grant agreement No. 101002511 - VEGA P). LW thanks the support from the one-hundred-talent project of Sun Yat-sen University, the Fundamental Research Funds for the Central Universities, Sun Yat-sen University (22hytd09) and the National Natural Science Foundation of China through grant 12073090 and 12233013. FA acknowledges financial support from MCIN/AEI/10.13039/501100011033 through grants IJC2019-04862-I and RYC2021-031638-I (the latter co-funded by European Union NextGenerationEU/PRTR). ST thanks Michela Mapelli for valuable comments and suggestions.

DATA AVAILABILITY

The data underlying this article will be shared on reasonable request to the corresponding authors.

REFERENCES

Aarseth S. J., 2003, Gravitational N-Body Simulations. Cambridge University Press, November 2003.
Alessandrini E., Lanzoni B., Ferraro F. R., Miocchi P., Vesperini E., 2016, ApJ, 833, 252
Almeida A., et al., 2023, arXiv e-prints, p. arXiv:2301.07688
Andrew S., Penoyre Z., Belokurov V., Evans N. W., Oh S., 2022, MNRAS, 516, 3661
Antonini F., Gieles M., 2020a, Phys. Rev. D, 102, 123016
Antonini F., Gieles M., 2020b, MNRAS, 492, 2936
Antonini F., Rasio F. A., 2016, ApJ, 831, 187
Askar A., Arca Sedda M., Giersz M., 2018, MNRAS, 478, 1844
Bahcall J. N., Wolf R. A., 1976, ApJ, 209, 214
Banerjee S., 2021, MNRAS, 500, 3002
Banerjee S., Belczynski K., Fryer C. L., Berczik P., Hurley J. R., Spurzem R., Wang L., 2020, A&A, 639, A41
Baumgardt H., 2001, MNRAS, 325, 1323
Baumgardt H., et al., 2019, MNRAS, 488, 5340
Belczynski K., Holz D. E., Bulik T., O'Shaughnessy R., 2016a, Nature, 534, 512
Belczynski K., et al., 2016b, A&A, 594, A97
Belokurov V., et al., 2020, MNRAS, 496, 1922
Boekholt T., Portegies Zwart S., 2015, Computational Astrophysics and Cosmology, 2, 2
Bovy J., 2015, ApJS, 216, 29
Cantat-Gaudin T., 2022, Universe, 8, 111
Cantat-Gaudin T., Anders F., 2020, A&A, 633, A99
Cantat-Gaudin T., et al., 2018a, A&A, 615, A49
Cantat-Gaudin T., et al., 2018b, A&A, 618, A93
Casamiquela L., et al., 2022, A&A, 664, A31
Casertano S., Hut P., 1985, ApJ, 298, 80
Castro-Ginard A., Jordi C., Luri X., Julbe F., Morvan M., Balaguer-Núñez L., Cantat-Gaudin T., 2018, A&A, 618, A59
Castro-Ginard A., et al., 2020, A&A, 635, A45
Castro-Ginard A., et al., 2022, A&A, 661, A118
Chen X., Amaro-Seoane P., 2017, ApJ, 842, L2
Chomiuk L., Strader J., Maccarone T. J., Miller-Jones J. C. A., Heinke C., Noyola E., Seth A. C., Ransom S., 2013, ApJ, 777, 69
Claydon I., Gieles M., Zocchi A., 2017, MNRAS, 466, 3937
Claydon I., Gieles M., Varri A. L., Heggie D. C., Zocchi A., 2019, MNRAS, 487, 147
Cropper M., et al., 2018, A&A, 616, A5
Dalton G., et al., 2012, in McLean I. S., Ramsay S. K., Takami H., eds, Society of Photo-Optical Instrumentation Engineers (SPIE) Conference Series Vol. 8446, Ground-based and Airborne Instrumentation for Astronomy IV. p. 84460P, doi:10.1117/12.925950
Di Carlo U. N., Giacobbo N., Mapelli M., Pasquato M., Spera M., Wang L., Haardt F., 2019, MNRAS, 487, 2947
Djorgovski S., King I. R., 1986, ApJ, 305, L61
Douglas S. T., Curtis J. L., Agüeros M. A., Cargile P. A., Brewer J. M., Meibom S., Jansen T., 2019, ApJ, 879, 100
El-Badry K., Burdge K. B., 2022, MNRAS, 511, 24
Evans N. W., Oh S., 2022, MNRAS, 512, 3846
Fleck J. J., Boily C. M., Lançon A., Deiters S., 2006, MNRAS, 369, 1392
Fryer C. L., Belczynski K., Wiktorowicz G., Dominik M., Kalogera V., Holz D. E., 2012, ApJ, 749, 91
Fukushige T., Heggie D. C., 2000, MNRAS, 318, 753
Gaia Collaboration et al., 2016, A&A, 595, A1
Gaia Collaboration et al., 2018a, A&A, 616, A1
Gaia Collaboration et al., 2018b, A&A, 616, A10
Gaia Collaboration et al., 2022, arXiv e-prints, p. arXiv:2208.00211
Geller A. M., Latham D. W., Mathieu R. D., 2015, AJ, 150, 97
Gieles M., Erkal D., Antonini F., Balbinot E., Peñarrubia J., 2021, Nature Astronomy, 5, 957
Giersz M., Heggie D. C., 2011, MNRAS, 410, 2698
Giesers B., et al., 2018, MNRAS, 475, L15
Giesers B., et al., 2019, A&A, 632, A3
Goodman J., 1984, ApJ, 280, 298
Goodman J., Heggie D. C., Hut P., 1993, ApJ, 415, 715
Heggie D. C., 1975, MNRAS, 173, 729
Hénault-Brunet V., Gieles M., Sollima A., Watkins L. L., Zocchi A., Claydon I., Pancino E., Baumgardt H., 2019, MNRAS, 483, 1400
Hills J. G., Fullerton L. W., 1980, AJ, 85, 1281
Hobbs G., Lorimer D. R., Lyne A. G., Kramer M., 2005, MNRAS, 360, 974
Hunt E. L., Reffert S., 2021, A&A, 646, A104
Hurley J. R., 2007, MNRAS, 379, 93
Hurley J. R., Pols O. R., Tout C. A., 2000, MNRAS, 315, 543
Hurley J. R., Tout C. A., Pols O. R., 2002, MNRAS, 329, 897
Jenet F. A., Creighton T., Lommen A., 2005, ApJ, 627, L125
Jerabkova T., Boffin H. M. J., Beccari G., de Marchi G., de Bruijne J. H. J., Prusti T., 2021, A&A, 647, A137
Kremer K., et al., 2020, ApJS, 247, 48
Kroupa P., 2001, MNRAS, 322, 231
Kulkarni S. R., Hut P., McMillan S., 1993, Nature, 364, 421
Kumamoto J., Fujii M. S., Tanikawa A., 2020, MNRAS, 495, 4268
Küpper A. H. W., MacLeod A., Heggie D. C., 2008, MNRAS, 387, 1248
Küpper A. H. W., Kroupa P., Baumgardt H., Heggie D. C., 2010, MNRAS, 401, 105
Küpper A. H. W., Lane R. R., Heggie D. C., 2012, MNRAS, 420, 2700

Lindegren L., et al., 2021, A&A, 649, A2
Liu L., Pang X., 2019, ApJS, 245, 32
Lodieu N., Smart R. L., Pérez-Garrido A., Silvotti R., 2019, A&A, 623, A35
Maccarone T. J., Kundu A., Zepf S. E., Rhode K. L., 2007, Nature, 445, 183
Mackey A. D., Wilkinson M. I., Davies M. B., Gilmore G. F., 2007, MNRAS, 379, L40
Mackey A. D., Wilkinson M. I., Davies M. B., Gilmore G. F., 2008, MNRAS, 386, 65
Madsen S., 2003, A&A, 401, 565
Makarov V. V., Odenkirchen M., Urban S., 2000, A&A, 358, 923
Mandel I., de Mink S. E., 2016, MNRAS, 458, 2634
Mapelli M., Colpi M., Possenti A., Sigurdsson S., 2005, MNRAS, 364, 1315
Meingast S., Alves J., 2019, A&A, 621, L3
Meingast S., Alves J., Rottensteiner A., 2021, A&A, 645, A84
Merritt D., 2001, ApJ, 556, 245
Merritt D., Piatek S., Portegies Zwart S., Hemsendorf M., 2004, ApJ, 608, L25
Miller-Jones J. C. A., et al., 2015, MNRAS, 453, 3918
Miralda-Escude J., 1996, ApJ, 470, L113
Miyamoto M., Nagai R., 1975, PASJ, 27, 533
Moe M., Di Stefano R., 2017, ApJS, 230, 15
Navarro J. F., Frenk C. S., White S. D. M., 1995, MNRAS, 275, 720
Nilakshi Sagar R., Pandey A. K., Mohan V., 2002, A&A, 383, 153
Odenkirchen M., et al., 2003, AJ, 126, 2385
Offner S. S. R., Moe M., Kratter K. M., Sadavoy S. I., Jensen E. L. N., Tobin J. J., 2022, arXiv e-prints, p. arXiv:2203.10066
Oh S., Evans N. W., 2020, MNRAS, 498, 1920
Paczynski B., 1996, ARA&A, 34, 419
Penoyre Z., Belokurov V., Wyn Evans N., Everall A., Koposov S. E., 2020, MNRAS, 495, 321
Penoyre Z., Belokurov V., Evans N. W., 2022, MNRAS, 513, 2437
Perryman M. A. C., et al., 1998, A&A, 331, 81
Peuten M., Zocchi A., Gieles M., Gualandris A., Hénault-Brunet V., 2016, MNRAS, 462, 2333
Piatti A. E., 2020, A&A, 639, A55
Pittordis C., Sutherland W., 2019, MNRAS, 488, 4740
Plummer H. C., 1911, MNRAS, 71, 460
Portegies Zwart S. F., McMillan S. L. W., 2000, ApJ, 528, L17
Rastello S., Amaro-Seoane P., Arca-Sedda M., Capuzzo-Dolcetta R., Fragione G., Tosta e Melo I., 2019, MNRAS, 483, 1233
Reino S., de Bruijne J., Zari E., d'Antona F., Ventura P., 2018, MNRAS, 477, 3197
Rodriguez C. L., Chatterjee S., Rasio F. A., 2016, Phys. Rev. D, 93, 084029
Röser S., Schilbach E., 2019, A&A, 627, A4
Röser S., Schilbach E., Piskunov A. E., Kharchenko N. V., Scholz R. D., 2011, A&A, 531, A92
Röser S., Schilbach E., Goldman B., 2019, A&A, 621, L2
Samsing J., et al., 2022, Nature, 603, 237
Sana H., et al., 2012, Science, 337, 444
Saracino S., et al., 2022, MNRAS, 511, 2914
Saracino S., et al., 2023, arXiv e-prints, p. arXiv:2303.07369
Sigurdsson S., Phinney E. S., 1993, ApJ, 415, 631
Sim G., Lee S. H., Ann H. B., Kim S., 2019, Journal of Korean Astronomical Society, 52, 145
Spitzer L., 1987, Dynamical evolution of globular clusters
Strader J., Chomiuk L., Maccarone T. J., Miller-Jones J. C. A., Seth A. C., 2012, Nature, 490, 71
Tarricq Y., Soubiran C., Casamiquela L., Castro-Ginard A., Olivares J., Miret-Roig N., Galli P. A. B., 2022, A&A, 659, A59
The LIGO Scientific Collaboration et al., 2021, arXiv e-prints, p. arXiv:2111.03606
Torniamenti S., Bertin G., Bianchini P., 2019, A&A, 632, A67
Torniamenti S., Rastello S., Mapelli M., Di Carlo U. N., Ballone A., Pasquato M., 2022, MNRAS, 517, 2953
Vesperini E., McMillan S. L. W., D'Antona F., D'Ercole A., 2013, MNRAS, 429, 1913
Vesperini E., Hong J., Webb J. J., D'Antona F., D'Ercole A., 2018, MNRAS, 476, 2731
Wang L., Hernandez D. M., 2021, arXiv e-prints, p. arXiv:2104.10843
Wang L., Jerabkova T., 2021, A&A, 655, A71
Wang L., Nitadori K., Makino J., 2020a, MNRAS, 493, 3398
Wang L., Iwasawa M., Nitadori K., Makino J., 2020b, MNRAS, 497, 536
Wang L., Tanikawa A., Fujii M. S., 2022, MNRAS, 509, 4713
Weatherford N. C., Chatterjee S., Kremer K., Rasio F. A., 2020, ApJ, 898, 162
Wen L., 2003, ApJ, 598, 419
Zhang Y., Tang S.-Y., Chen W. P., Pang X., Liu J. Z., 2020, ApJ, 889, 99
Zocchi A., Gieles M., Hénault-Brunet V., 2019, MNRAS, 482, 4713
de Jong R. S., et al., 2019, The Messenger, 175, 3
de Vita R., Bertin G., Zocchi A., 2016, A&A, 590, A16
van Straten W., Bailes M., Britton M., Kulkarni S. R., Anderson S. B., Manchester R. N., Sarkissian J., 2001, Nature, 412, 158

This paper has been typeset from a TEX/LATEX file prepared by the author.

sourceid	RA	Dec	parallax	pmra	pmdec	mg	bprp	RUWEast	sigmabast	RUWEspec	sigmabspec	P	q	$M_{\rm c}$
3313842529024545664	65.85493019594335	16.7771474657318 76	20.795046	106.97092	-26.247469	5.573977	0.40038252	1.2823561	0.41557395	27.358295	23.794285	0.025030272	0.44117424	0.6805129
3311000119668435200	65.51518023603637	14.077103275227195	22.026937	113.774475	-21.321016	5.6442456	0.42680836	1.8872856	0.7889371	19.065733	14.198232	0.075180255	0.3714967	0.5546593
3309990523179108480	69.53972879902068	16.03321720295417	17.820915	84.96662	-8.793861	5.7026787	0.4365778	5.6922646	2.4559207	2.1845562	1.2523471	3.2795131	0.09720816	0.15520167
3312637842237882880	67.96612153925633	15.851471350184573	21.005054	99.49563	-34.32999	5.928877	0.46518755	1.5450443	0.47656766	2.0089986	0.8186548	0.82594234	0.039998896	0.057937805
14413051681679200	67.57532736919829	19.84041406012967	19.89243	86.11872	-26.106121	6.9827037	0.6383934	3.7624655	1.3966898	3.2055814	0.9599861	2.179701	0.069570266	0.08619921
3312751882209460864	66.52490368958763	15.524230392191061	23.521027	124.196014	-25.313429	7.3494782	0.7129674	3.4419775	1.343747	2.0151875	0.5174881	3.2901115	0.044089917	0.04835587
3309493720019304576	69.38373895275495	15.146378860785259	25.64366	101.49229	-18.512648	7.4436464	0.7864218	13.72717	5.776902	9.669819	2.558703	2.6238859	0.2289321	0.23954499
3311151233797884416	66.05246947657736	14.758157583423541	20.856197	110.226265	-12.401878	7.4817166	0.7890749	4.709577	1.9607697	2.121658	0.4972577	5.634556	0.05053243	0.056626927
3307815006281475200	67.87268564180225	13.903399057854472	20.276747	86.607285	-6.108541	7.643193	0.69734	8.31893	3.525965	2.614277	0.7415865	6.9882374	0.083096355	0.09157219
3309170875916905856	69.73925748852255	14.105477042258816	18.390837	91.53597	-20.422842	7.8071556	0.80762196	10.741918	4.6240096	3.6913257	1.0178571	7.361735	0.118229695	0.1313378
3313743710417140864	66.60303643900508	16.853180488088583	26.757921	95.673996	-38.761845	7.8861456	0.81799173	12.058122	5.1952686	10.748748	3.0819666	1.8774892	0.25809193	0.24698886
3309006602007842048	71.62700947833584	15.471931785895292	20.5006	87.325676	-25.352728	8.138844	0.8205805	3.2997699	1.3771452	2.1922784	0.5878727	3.40549	0.052342582	0.052890003
3309540170088830464	68.49438499286096	15.16352719505778	20.641268	108.03673	-33.110138	8.2856655	1.0252385	27.214418	11.50729	5.577302	1.5087116	11.012355	0.22136614	0.2177251
48061409893621248	67.1555527872302	19.74051990049017	20.810343	102.9064	-38.101357	8.441752	0.89888763	1.6440603	0.53488284	14.239208	4.5749774	0.16743268	0.16246925	0.15522723
3312631623125272448	67.64578394363194	15.733880135447295	17.485168	100.58648	-25.256905	8.67361	1.0493889	21.024082	7.626148	18.202843	5.276344	2.4634974	0.55225676	0.54067534
48197783694869760	65.84566930782594	19.658531350570186	21.598646	97.3178	-37.780178	9.1158905	1.1155329	34.355576	10.966481	16.315971	5.2403026	2.887581	0.62754923	0.52858657
3314151251273992832	67.9051025367819	17.70963694563987	28.507998	98.723816	-22.038061	9.247976	1.1795635	43.27126	13.478946	17.999285	5.767014	2.443363	0.70073265	0.5220939
3406216383523959936	70.81584857548913	17.068982088574	22.40773	84.4349	-41.66873	9.519791	1.2086744	14.337425	4.4526625	2.7862427	0.90990114	6.508449	0.11398687	0.08856268
47319858019739264	64.59216618931373	17.421415275740294	23.752161	104.46378	-50.567753	9.66315	1.3945608	10.326841	3.221443	2.0533266	0.5846881	6.9130993	0.07403989	0.054991435
3314484094059409408	66.99617799986078	18.500100518411095	19.760468	108.59516	-40.885216	9.7873955	1.2999792	10.631993	3.3175225	4.8615503	1.7125669	2.9215875	0.1696449	0.13192531
3310876802567157248	66.85605547720428	14.260578556388577	20.42228	102.45836	-19.95602	10.026131	1.33076	12.669773	3.9585905	4.7959375	1.7974386	3.2138977	0.18906817	0.13960828
3308127405023027328	70.3740966937844	13.221124178946916	22.662909	99.23287	-18.63009	10.491406	1.8964214	1.4050351	0.29435474	5.7457695	2.2721488	0.1703603	0.08793274	0.057852447
3410898202818634624	68.70917414686971	20.394419352148518	18.76046	110.18581	-22.617853	10.571909	1.6212931	9.876004	2.8892152	8.526632	3.900182	1.1767963	0.32126498	0.2233311
3313526556869575296	66.20070596676636	15.874649203665436	20.678333	100.34452	-12.269188	11.324224	1.9229269	12.951795	4.8260064	3.9638534	2.295628	3.0298467	0.2657315	0.15727599
3314185129975960448	67.12038862642493	17.695791947186837	20.918434	109.48695	-44.22729	11.360385	2.2351828	15.092351	5.5574145	8.521062	4.8796754	1.6225665	0.52000636	0.3046414
3312751229374292864	66.45571421241527	15.521152733202104	19.244942	118.904	-10.06363	11.395764	1.9788427	13.038091	4.7377243	8.969254	5.425513	1.3522661	0.54579365	0.32762027
3309541170817293824	68.66689038204488	15.208964911975178	21.075073	103.15689	-35.85557	11.549942	2.0912971	3.344131	1.0991819	6.668379	4.2592897	0.36493292	0.2443392	0.13831078
3309336867813205760	68.52256353868661	14.21747714186208	18.199448	85.34915	-16.904617	11.629388	1.8422108	1.4415438	0.34694323	2.4431305	1.6714453	0.3399052	0.08429948	0.049661882
47917816253918720	66.31113667576857	18.973455972926324	18.569708	97.28108	-28.887608	11.957183	2.0487833	2.0377967	0.5246777	8.945428	7.500937	0.11225916	0.30151984	0.16694689
3313958046465282304	66.30695338557209	17.268076545714347	19.312836	107.2612	-27.188425	11.998245	2.6850185	9.333254	2.704557	26.169952	19.287603	0.2163822	1.5024871	0.81455195
3308152208457011072	71.33211010053422	13.574216271157622	19.19447	87.72377	-9.913272	12.024581	2.3941412	15.202123	4.3817663	9.862589	7.8390193	0.86788297	0.77107835	0.41712388
3311162843092490496	65.96041133865042	14.921402707495972	25.659887	113.94731	-28.725637	12.134732	2.6072578	11.986289	3.3206553	5.654087	4.5110784	0.85494554	0.39180115	0.18730214
3307489031146701696	68.36303444839065	13.045385968619557	23.333511	110.45561	-21.440964	12.256755	2.342475	1.363789	0.2545818	2.3844779	2.0315888	0.16005203	0.08510464	0.041261565
3308428877366857728	70.36635522147463	14.076016738839469	26.182947	99.25034	-33.95699	12.363147	2.4602451	25.720503	7.026489	10.856859	10.731864	0.745237	1.2423422	0.56752026
3410409886514680064	69.01782417867581	18.888423253705223	20.245579	84.23755	-22.036737	12.484824	2.47365	6.511168	1.7505827	11.434649	12.022853	0.21433577	0.76413935	0.3754725
47729215646206080	64.46150286122511	18.475053544960033	21.640215	113.170876	-30.777138	12.703422	2.6998405	2.711683	0.7202027	2.0415013	2.0097606	0.49351305	0.12772296	0.059066143
48455894049191424	63.624805023608	18.729881346946026	20.680376	110.10128	-30.568058	13.204377	2.7620544	3.769246	0.98915327	4.831599	7.9032397	0.18036395	0.43028054	0.18605632
49157794854448192	65.67911798706223	20.56998136359179	22.204473	109.14224	-37.47773	13.435896	2.8771925	10.13076	2.8767006	4.160689	7.6917205	0.50197315	0.66635245	0.2701574
3312613000147191680	67.93658293586253	15.630149907181586	21.92811	104.99937	-31.718637	13.436778	2.7022161	1.2680652	0.22256374	2.1944704	4.0981297	0.073810354	0.14576809	0.059358526
3311038666998173184	65.84974595899124	14.427849817287893	21.160046	110.94352	-21.135527	13.543492	2.9259453	12.498561	3.6824527	20.370281	41.5711	0.12476101	5.761253	2.334608
3313207698500079360	69.63189917287164	17.04055509824066	22.853317	106.24673	-31.3891	13.618415	2.808816	1.2659032	0.23495989	4.2582116	9.578849	0.031987548	0.282138	0.109801285
3314140599755959424	67.60020695729807	17.499587834144798	18.23571	78.77907	-28.804348	13.654834	2.7426186	10.872717	3.3146904	2.9538498	6.8027906	0.79631144	0.6842594	0.28725055
3313839574086963712	65.39849909000245	16.894192274532255	24.33773	125.71914	-40.65925	13.948855	3.064352	8.383781	2.817	5.9499407	14.526592	0.23746127	1.244193	0.44788775
3310478710637066752	64.53629289150157	13.331259196596612	20.93439	111.15798	-14.546099	13.949699	2.8872652	1.5854778	0.4164988	4.107172	10.453021	0.056723293	0.3978708	0.15124361
3314137846679343872	68.0336649745617	17.6643440638911	21.075275	99.88685	-30.655151	13.979582	2.8372974	1.5255272	0.3941187	2.4364855	6.2334156	0.08940822	0.25801963	0.097356565
47760521664503296	65.11560537190881	18.89705576636259	19.672964	104.719475	-32.569706	13.988257	2.7881794	1.2785263	0.27335688	2.2563696	5.902441	0.070158176	0.21893603	0.08457476
3311221258944195200	65.66660974089085	15.062399584369444	23.376665	84.40576	-23.434784	14.077939	3.0911245	1.3902847	0.34179467	3.8369422	9.311588	0.046796	0.32785812	0.11720649
48509186003340416	62.776059616737115	18.928963628615932	19.93843	109.657745	-28.472279	14.192208	2.9350224	1.7115903	0.5110402	3.5404887	11.017797	0.069329664	0.46646634	0.17331943
48048902948906368	66.90245867179468	19.445767441293732	19.231146	96.80087	-38.773808	14.238761	3.0310307	16.237202	6.0698442	3.4705567	9.437445	0.99670756	1.3147694	0.4911199
3311102820926310784	65.39669553192954	14.695153868168017	20.326693	106.496574	-19.731718	14.278773	2.862668	1.3977338	0.3713231	2.7254941	9.875319	0.05512948	0.37344685	0.1358137
3311810047420637568	63.46857579356195	15.364870633400007	22.387419	123.95292	-13.587856	14.308949	2.9282503	1.5574532	0.4591437	5.319673	20.914965	0.029223839	0.7675065	0.26816785
3311804515502788352	63.273952149488956	15.247700118856342	22.357246	122.44951	-18.603453	14.355454	2.9613495	1.3029861	0.32675368	2.5205526	10.018484	0.04347603	0.35185495	0.12204755
47322297561027712	64.65025269592638	17.51585330705525	27.013884	64.83592	-61.09387	14.369595	2.959774	1.2812126	0.31491673	2.0114625	7.8232236	0.04440918	0.27206907	0.08790898
45198178534988672	62.49039974488908	15.416883616520483	21.22679	118.5227	-21.854282	14.58098	3.1423988	1.5162789	0.48248684	4.441856	20.385468	0.03322999	0.7961063	0.27099073
3410559832411244160	69.96546164739077	19.6593898461387	23.499067	87.291985	-34.15228	14.677451	3.234291	16.270372	7.1377497	3.6114807	11.025825	0.8210118	1.6573471	0.5350476
47959705067457152	66.12800628155945	18.986786982710726	20.498665	111.01914	-43.00263	14.982163	3.2060423	10.618676	5.2158256	2.239869	10.304867	0.7358764	1.3935447	0.44927633

Table 5. Candidate binaries in the Hyades with significant astrometric and spectroscopic excess noise. RA and Dec are in degrees - sigmabspec is in kms^{-1} - all other quantities are expressed in the appropriate combinations of mas, yr and $M_{\odot}$.